ARMY RESEARCH LABORATORY

Hot Explosive Consolidation of Molybdenum-Titanium and Tungsten-Titanium Alloys

by Laszlo J. Kecskes

19981026 051

Abstract

A novel hot explosive compaction (HEC) technique has been applied to molybdenum (Mo)- and tungsten (W)-based titanium (Ti) alloys. The constituent precursor powders of the alloy billet were surrounded by an exothermic mixture, which, when ignited, released a large amount of heat via a self-propagating high-temperature synthesis (SHS) reaction. Heat from the SHS reaction diffused into the precursor powder bed, causing the interior temperature to rise above 1,500° C. When the powder bed became isothermal, it was consolidated to high density by pressure waves generated by the detonation of an explosive. The amount of explosive charge and the molar ratio of exothermic mixture to sample were adjusted to produce full-density molybdenum-titanium (Mo-Ti) and tungsten-titanium (W-Ti) alloys. The billets were sectioned and examined with scanning electron microscopy (SEM), energy dispersive x-ray spectroscopy (EDS), x-ray diffraction analysis (XRD), and microhardness measurements. In context of the fabrication process, the similarities and differences of the resultant product microstructures are discussed.

Acknowledgments

INTENTIONALLY LEFT BLANK.

Table of Contents

INTENTIONALLY LEFT BLANK.

List of Figures

INTENTIONALLY LEFT BLANK.

List of Tables

INTENTIONALLY LEFT BLANK.

1. Introduction

High tungsten (W) content alloys continue to present considerable challenges to the powder metallurgy industry. Because W has the highest melting point among metals, T_m = 3,380° C, its alloys, especially those with transition metal elements, are most effectively produced by liquid-phase sintering (LPS) [1]. Over the last 10–15 yr, LPS has focused on the development of two-phase tungsten heavy alloys (WHA) with a nickel-iron or copper-nickel matrix for use in military applications. Renewed interest in the extension of LPS technology has centered on matrix metals such as titanium (Ti), Ti-6Al-4V alloys, zirconium (Zr), hafnium (Hf), and steel [2]. However, the presence of brittle intermetallic phases in the systems with Zr, Hf, and iron [3] limits their applicability and utilization. In addition to LPS, solid-state sintering, extrusion, and mechanical alloying [4], the use of explosive compaction to consolidate and sinter the powdered precursors has been examined [5].

During the past three decades, explosive compaction has been extensively applied to metal and ceramic powders. When an explosive, adjacent to a powder sample, is detonated, a shock wave propagates through and densifies the powder bed. Bonding is produced via localized heating between neighboring particles as they slide past one another. Due to the rapid densification rate, the samples often suffer from low nonuniform densities, poor interparticle bonding, and severe cracking. The rise in temperature, associated with the irreversible work occurring during the consolidation of distended solids, has frequently been found to be insufficient to develop adequate bonding. To overcome some of these problems, hot explosive compaction (HEC) has been suggested [6–11], where preheating is used to decrease the yield strength of the powder, thereby improving its ductility.

Recently, W-based alloys [5] have been consolidated with a variant of HEC at the U.S. Army Research Laboratory (ARL). This technique, referred to hereafter as combustion synthesis assisted (CSA)-HEC, uses an in situ self-propagating high-temperature synthesis (SHS) reaction (i.e., "chemical furnace") to preheat the powder sample prior to compaction. Chemical heating [12]

1

and thermite mixtures [13] have already been used to heat samples prior to shock loading. Admixed exothermic mixtures have also been shock initiated to locally enhance sample properties [10, 11].

The chemical furnace is a highly exothermic mixture of reactant powders that, when initiated, will generate heat and provide high temperatures. SHS has been extensively researched in the former Soviet Union, Japan, and the United States [14–16].

This effort was designed to explore the feasibility of applying the CSA-HEC technique to molybdenum (Mo)-Ti and W-Ti powder mixtures. The general features of the phase diagrams of the Mo-Ti and W-Ti systems are very similar, with the exception of a substantially lower melting point for Mo, T_m = 2,620° C vs. T_m = 3,380° C for W. Therefore, the influence of the proximity of the chemical furnace, peak interior temperature, and rate of preheating on the sample structure were of primary concern. The extent of dissolution and dispersion of the Mo grains, compared to those of W, in the Ti matrix was also of interest. The billets were sectioned and examined with scanning electron microscopy (SEM), energy dispersive x-ray spectroscopy (EDS), x-ray diffraction (XRD) analysis, and microhardness measurements. In context of the CSA-HEC fabrication process, the similarities, differences, and evolution of the resultant product microstructures are discussed.

2. Experimental Procedure

The precursor powders used in these experiments were –325 mesh (equivalent to –44 µm), 99.9% pure Mo (CERAC, Inc., Milwaukee, WI); 12 µm, 99.9% pure W (Johnson Matthey, Ward Hill, MA); –325 mesh, 99.5% pure Ti (Micron Metals, Salt Lake City, UT); and 2 µm, 99.9% pure graphite (CERAC, Inc., Milwaukee, WI). The component powders were blended in a prescribed mass ratio. A mass ratio of 90:10 was used in the Mo+Ti mixture, and a mass ratio of 95:5 was used in the W+Ti mixture. In this manner, the atomic ratios of the constituents were approximately the same in both mixtures; for the Mo+Ti mixture, it was 82:18, and for the W+Ti mixture, it was 83:17. Each mixture was ball-milled for several hours and stored in argon until the CSA-HEC experiment was performed. For comparison, the unalloyed metal powders were compacted as well. In the

2

remainder of the discussion, only mass ratio designations are used. Conversion tables for the Mo-Ti and W-Ti systems are provided in Appendices A and B. The Ti and graphite (C) powders used in the SHS chemical furnace were mixed with a Ti:C molar ratio of 1.0 for maximum heat release. This Ti+C mixture was pressed into doughnut-shaped green compacts.

As shown in Figure 1, SEM of the Mo revealed polyhedral particles, with a coarse surface texture, ranging in size from 10 to 30 µm. The W particles were polyhedral and faceted, ranging in size from 5 to 20 µm. The Ti was irregular, having faceted to elongated shapes, with a size range of 10 to 40 µm. The C powder was excluded from a microscopic examination, since it had no direct effect on the alloy structure.

Figure 2 shows the schematic of the CSA-HEC reaction vessel, which functions not only to contain the SHS reaction but also as the explosive compaction fixture. The reaction vessel and explosive driver package were assembled separately. The driver package was affixed onto the vessel and the completed fixture placed on a sandpile. The Ti+C→TiC SHS reaction was ignited remotely, and as the reaction proceeded to completion (3 s), the generated heat diffused into the powder bed. The outside of the Mo+Ti or W+Ti powder bed heated up rapidly while its interior lagged behind. As the periphery began to cool and the interior continued to heat up, at 60 to 65 s, the powder bed was isothermal. During this condition, the anvil was activated by the detonation of the explosive to densify both the sample and the TiC doughnut. The fixture was buried under sand, which protected the case and contents from excessive thermal shock. After cooling to ambient temperatures, the alloy billet was extracted.

Experiments were carried out to measure the sample temperature and rate of heating in the reaction/compaction fixture during the preheating phase of the process. As shown in Figure 3, for these experiments, the reaction/compaction fixture was modified by removing the explosive container and inserting a series of equally spaced W-Rhenium thermocouples into the middle of the Mo+Ti sample through the base of the fixture. After the TiC reaction was initiated, the emf output of the thermocouples was recorded as a function of time using Labtek Notebook (a PC-based, data acquisition system) until the fixture cooled to ambient temperature.

3
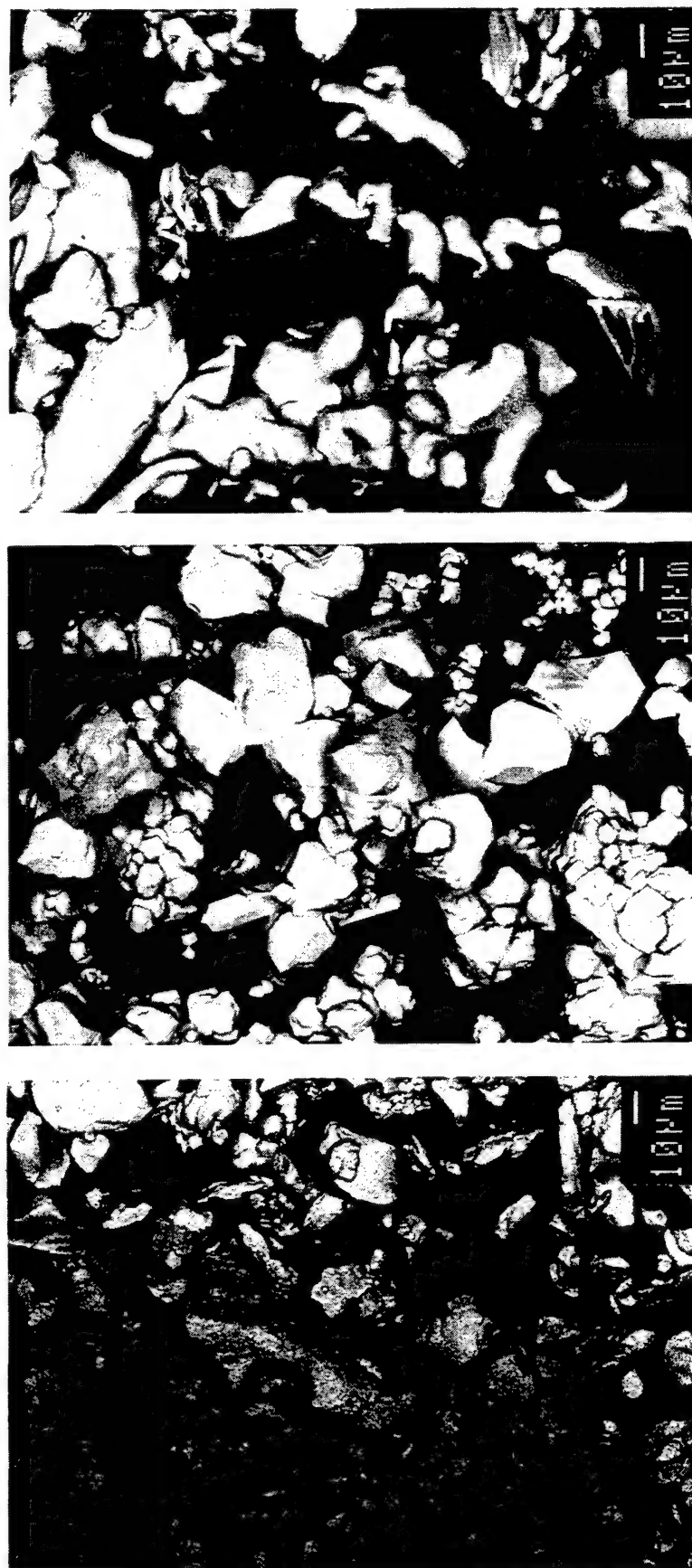
Figure 1. Scanning Electron Micrographs of the Precursor Powders: (a) Mo, (b) W, and (c) Ti.

4
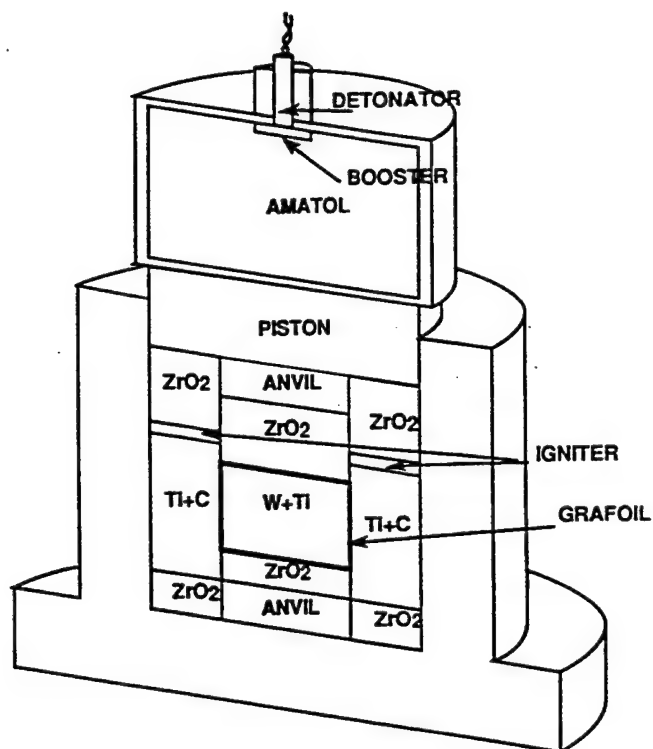
Figure 2. Schematic Diagram of the CSA-HEC Fixture.
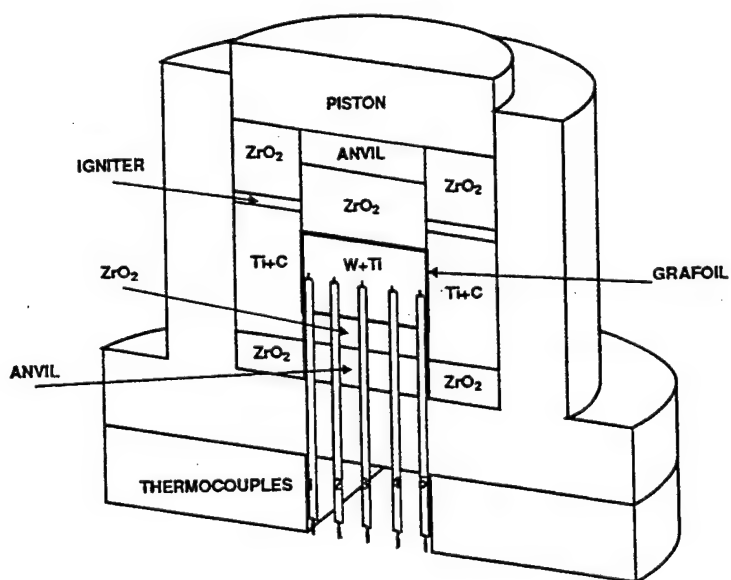
Figure 3. Schematic Diagram of the Modified CSA-HEC Fixture Used in the Temperature Measurements.

5

Full-density CSA-HEC metal and alloy samples were fabricated with explosive charge mass to piston/anvil mass values (c:m) of about 1.7–2.2. The CSA-HEC experiments were conducted with n_{TiC}:n_s values (ratio of moles of exothermic compound to moles of sample) of 5.6–6.2.

The uniformity of compaction of the billets was evaluated by density measurements and optical microscopy. Samples were cut and prepared for SEM, EDS, and XRD analysis. The SEM samples were mounted and diamond polished to a 1/4-µm finish. X-ray diffraction samples were polished to remove any surface damage introduced during cutting and mounted into standard aluminum (Al) x-ray diffractometer sample holders. To obtain a precise measure of the lattice parameter of the phases present, the linear intercept method was used [17]. Fracture surfaces, generated by impact loading, from the core region of the billets were examined with SEM for a qualitative examination of intergrain bonding. Vickers microhardness measurements were performed with 100-gf and 400-gf loads. Listed values represent the average of 20 individual hardness measurements with a limit of error of ±0.15 GPa. Further details of the CSA-HEC process and experimental procedures are in Kecskes and Hall [5].

3. Results and Discussion

The phase diagrams of the two systems are shown in Figure 4. The Mo-Ti system is in Figure 4(a), and the phase diagram of the W-Ti system is in Figure 4(b) [3]. Both of the metals exhibit limited solubility in α-Ti, and the systems contain a critical point and a monotectoid reaction. The critical point at 850° C, 50Mo-50Ti, for the Mo-Ti system, corresponds to the decomposition of β-Ti/Mo $\leftrightarrow$ β-Ti + Mo. The monotectoid reaction of β-Ti/Mo $\leftrightarrow$ α-Ti + Mo, is at 695° C, 22Mo-78Ti. The features for the W-Ti system appear at higher temperatures. The critical point, at 1,250° C, 65W-35Ti, corresponds to β-Ti/W $\leftrightarrow$ β-Ti + W. The monotectoid reaction β-Ti/W $\leftrightarrow$ α-Ti + W is at 740 ±20° C, 28W-72Ti. While the specific temperatures and compositions are different, based on the overall features of the equilibrium-phase diagrams of the two systems, their behaviors are expected to be similar.
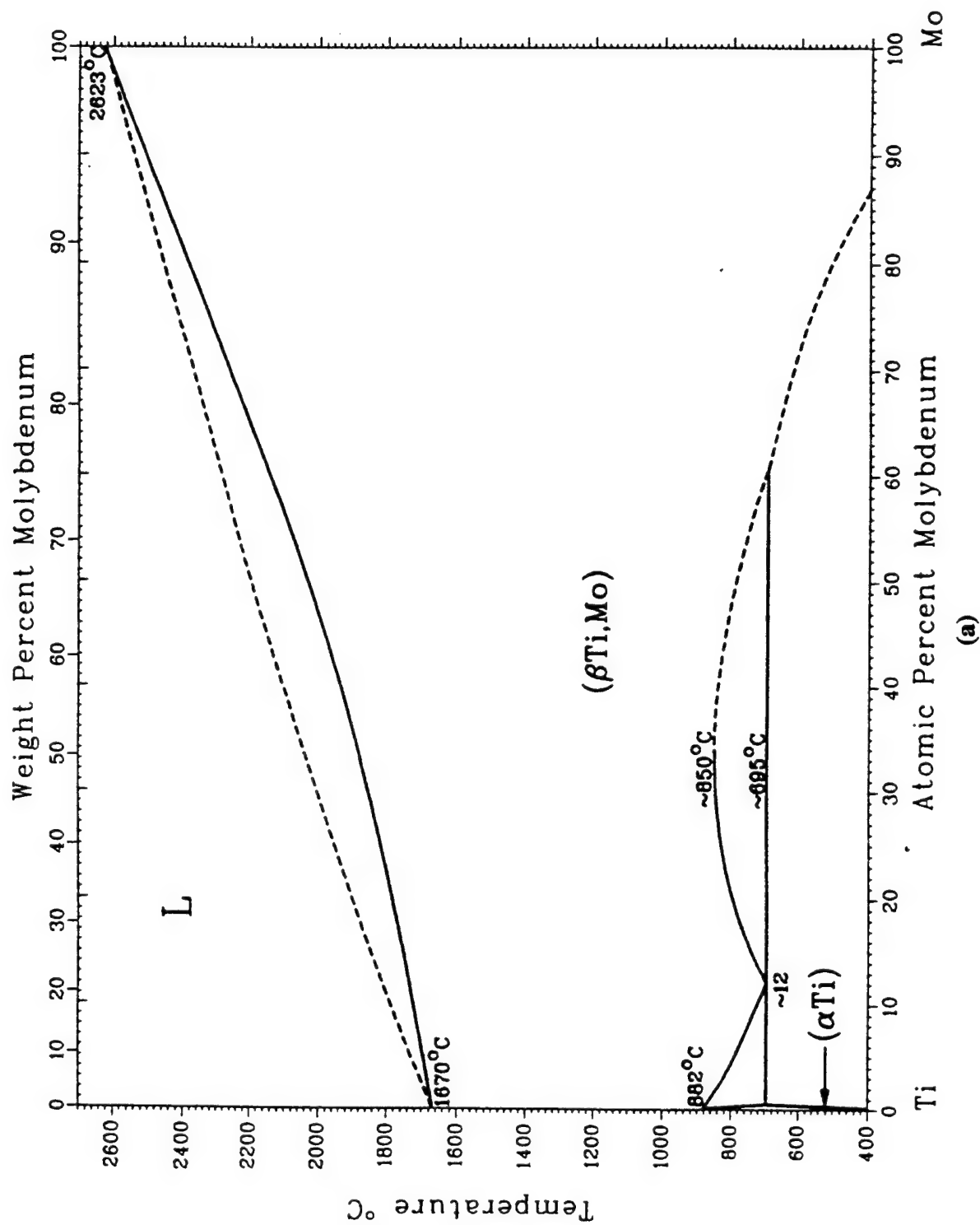
Figure 4. Equilibrium Phase Diagrams of the (a) Mo-Ti System and (b) W-Ti System. From Massalski et al. [3].
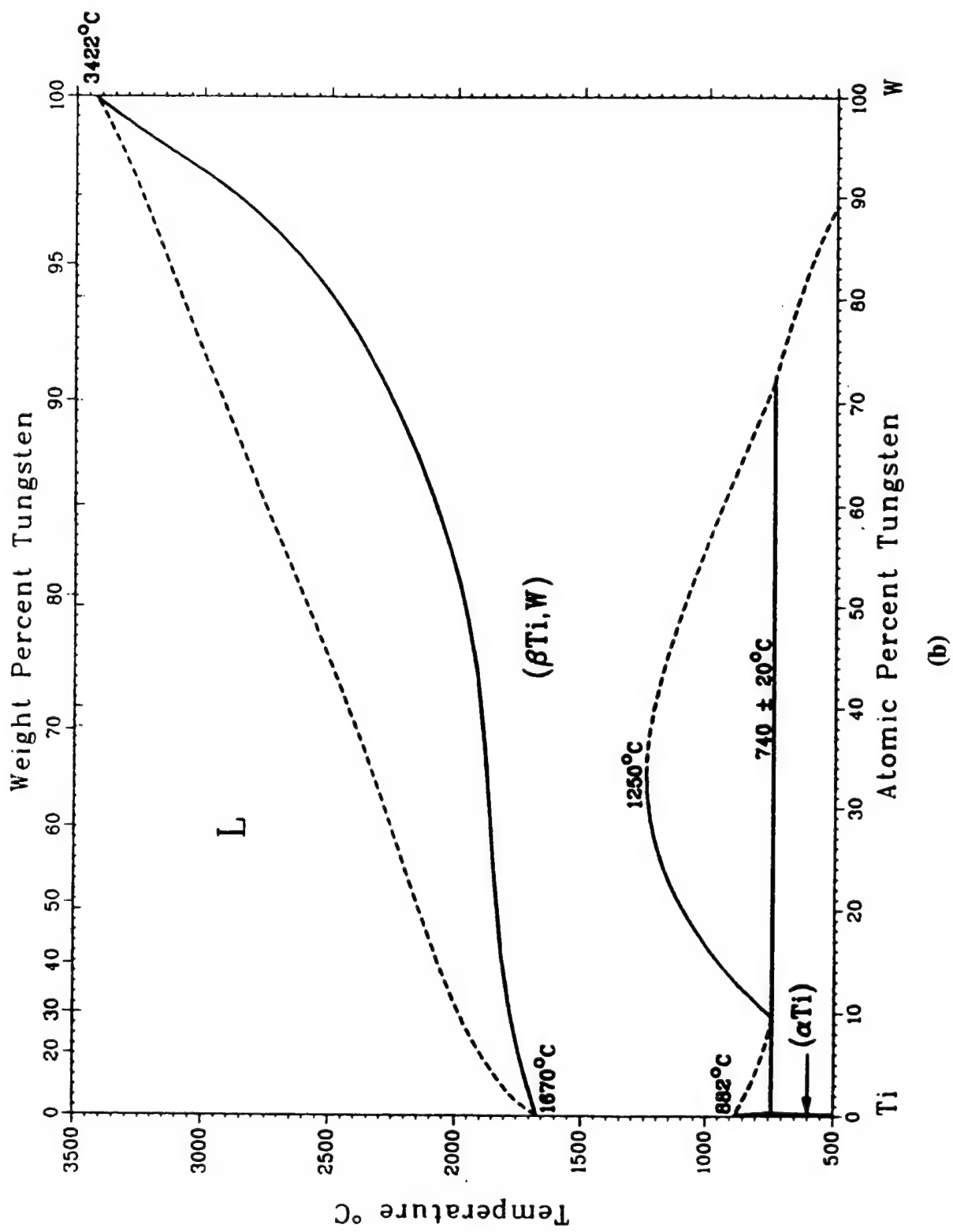
Figure 4. Equilibrium Phase Diagrams of the (a) Mo-Ti System and (b) W-Ti System. From Massalski et al. [3] (Continued).

8

3.1 Temperature Measurements. Precompaction temperature-time data measurements, supported by adiabatic heat balance calculations, indicated that the n_{TiC}:n_s value significantly affected the heating rates and peak temperatures attained within the sample. For best results, the n_{TiC}:n_s value was adjusted so that as much of the bulk of the sample would be near, but not exceed, the melting point of Ti, $T_m = 1,670°$ C, and excessive overheating of the periphery would be minimized. However, unless a large enough n_{TiC}:n_s value was used, the sample did not become isothermal at a sufficiently high temperature at any point during the preheating cycle. The n_{TiC}:n_s value of about six satisfied both of these criteria.

The measurements of the sample temperature during the preheating phase were essential in the consolidation of the CSA-HEC samples. The results are shown in Figure 5. The data for 90Mo-10Ti are in Figure 5(a), and the data for 95W-5Ti are in Figure 5(b). The pair of vertical arrows marks the duration of the Ti+C reaction. For both cases, the temperature in the outer periphery rises rapidly, exceeding 2,000° C, then asymptotically decreases. The rate of temperature increase in the midregion and interior of the bed is more gradual, reaching only a temperature of about 1,550° C. This temperature is close to, but does not exceed, the T_m Ti. At approximately 60–65 s after the initiation of the TiC reaction, the cooling of the periphery and the heating of the interior converge such that the powder bed is isothermal. After this isothermal plateau, the powder bed begins to cool slowly. Overall, aside from a more sluggish rise in the interior of the powder bed, the Mo-Ti system exhibited the same temperature response as the W-Ti system. Note that the slower temperature rise reduces the duration of preheating in the interior of Mo-Ti. The thermal response of the CSA-HEC system is interpreted as follows.

As shown by Equations 1(a), 1(b), 2(a), and 2(b), the maximum allowable temperature rise in the sample is determined by the balance between the amount of heat generated by the TiC SHS reaction, ΔH_{rxn}^{TiC}, and the amount of heat absorbed by the TiC furnace and the Mo+Ti or W+Ti sample. Because the surrounding steel fixture is identical in all CSA-HEC experiments, its contribution to the adiabatic heat balance would be expected to be the same. Therefore, it was felt that its inclusion in the heat balance was not warranted. The thermodynamic data and heat capacity coefficients are listed in Appendix C.
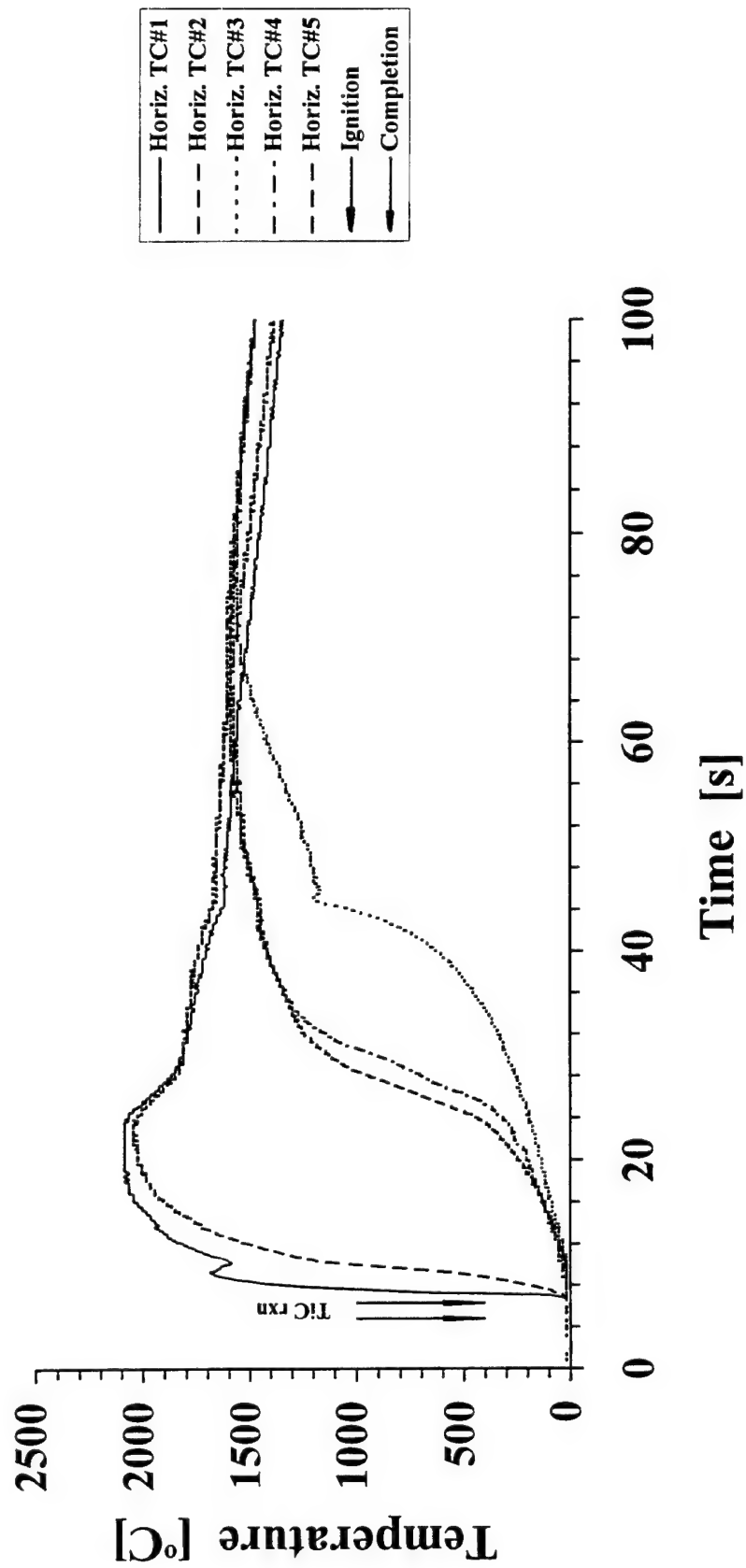
Figure 5. Results From the Temperature Measurement for the CSA-HEC Preheating Phase: (a) 90Mo-10Ti and (b) 95W-5Ti.

Figure 5. Results From the Temperature Measurement for the CSA-HEC Preheating Phase: (a) 90Mo-10Ti and (b) 95W-5Ti (Continued).

11
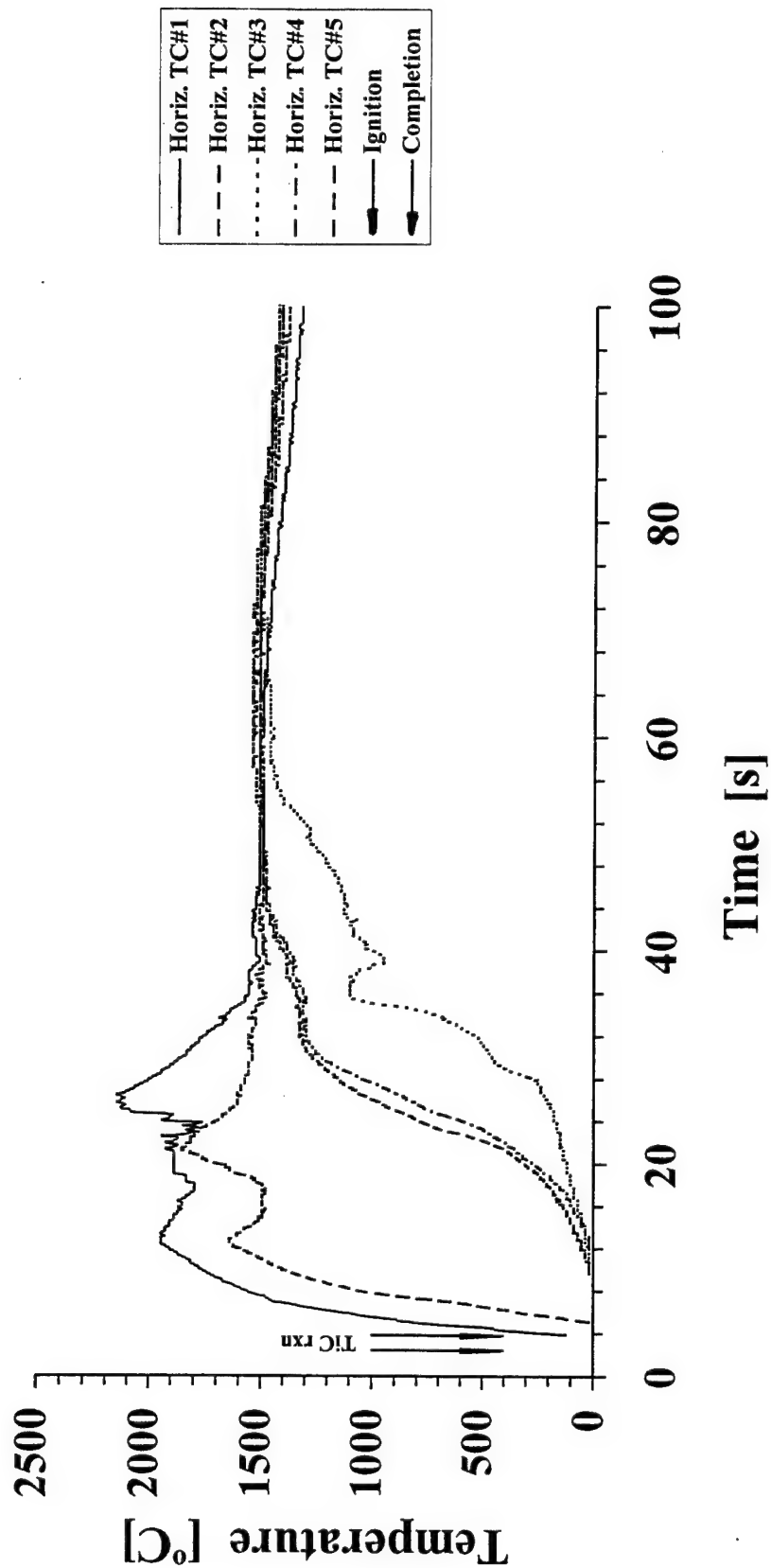
$$n_{TiC}\left(\Delta H_{rxn}^{TiC} - C_p^{TiC}\Delta T\right) = n_s\left[x_{Mo}C_p^{Mo}\Delta T + x_{Ti}\left(C_p^{Ti}\Delta T + L_\beta^{Ti} + L_{\beta\to liq.}^{Ti}\right) + x_{air}C_p^{air}\Delta T\right]. \tag{1a}$$

$$\frac{n_{TiC}}{n_s} = \frac{x_{Mo}C_p^{Mo}\Delta T + x_{Ti}\left(C_p^{Ti}\Delta T + L_{\alpha\to\beta}^{Ti} + L_{\beta\to liq.}^{Ti}\right) + x_{air}C_p^{air}\Delta T}{\Delta H_{rxn}^{TiC} - C_p^{TiC}\Delta T}. \tag{1b}$$

$$n_{TiC}\left(\Delta H_{rxn}^{TiC} - C_p^{TiC}\Delta T\right) = n_s\left[x_W C_p^W\Delta T + x_{Ti}\left(C_p^{Ti}\Delta T + L_{\alpha\to\beta}^{Ti} + L_{\beta\to liq.}^{Ti}\right) + x_{air}C_p^{air}\Delta T\right]. \tag{2a}$$

$$\frac{n_{TiC}}{n_s} = \frac{x_W C_p^W\Delta T + x_{Ti}\left(C_p^{Ti}\Delta T + L_{\alpha\to\beta}^{Ti} + L_{\beta\to liq.}^{Ti}\right) + x_{air}C_p^{air}\Delta T}{\Delta H_{rxn}^{TiC} - C_p^{TiC}\Delta T}. \tag{2b}$$

The heat absorbed by the samples includes the contributions from the molar heat capacities of the residual porosity, C_p^{air}, and the component powders (solid or liquid), C_p^{Ti}, C_p^{Mo}, or C_p^W, and the latent heats of phase transitions, $L_{\alpha\to\beta}^{Ti}$, and $L_{\beta\to liq.}^{Ti}$, that may occur during preheating (i.e., up to 2,000° C or 2,300 K). Neither W nor Mo undergoes any phase transitions within this temperature range, but those of Ti, $\alpha \to \beta$ at 882° C, and $\beta \to$ liq. at 1,670° C, must be considered. Using the rule of mixtures, the overall heat capacity of the sample is the weighed sum of its components. The weighing factor is the mole fraction. Since the mole fraction of Ti, x_{Ti}, is the same in both systems, its molar heat capacity contribution to that of the total in each system is identical. The molar heat capacities of W and Mo are comparable over the preheating temperature range, so the contribution from W or Mo to the total heat capacity is essentially the same. Finally, because the packing densities of the powder beds are roughly equal, the contribution from the porosity is also the same in both cases. Then, with the other terms being the same, it may be concluded that for a given value of n_{TiC}:n_s, the maximum attained temperature in the powder bed is approximately the same for either of these compositions. As shown in Figure 6, calculations for the interior temperatures are consistent with this hypothesis.
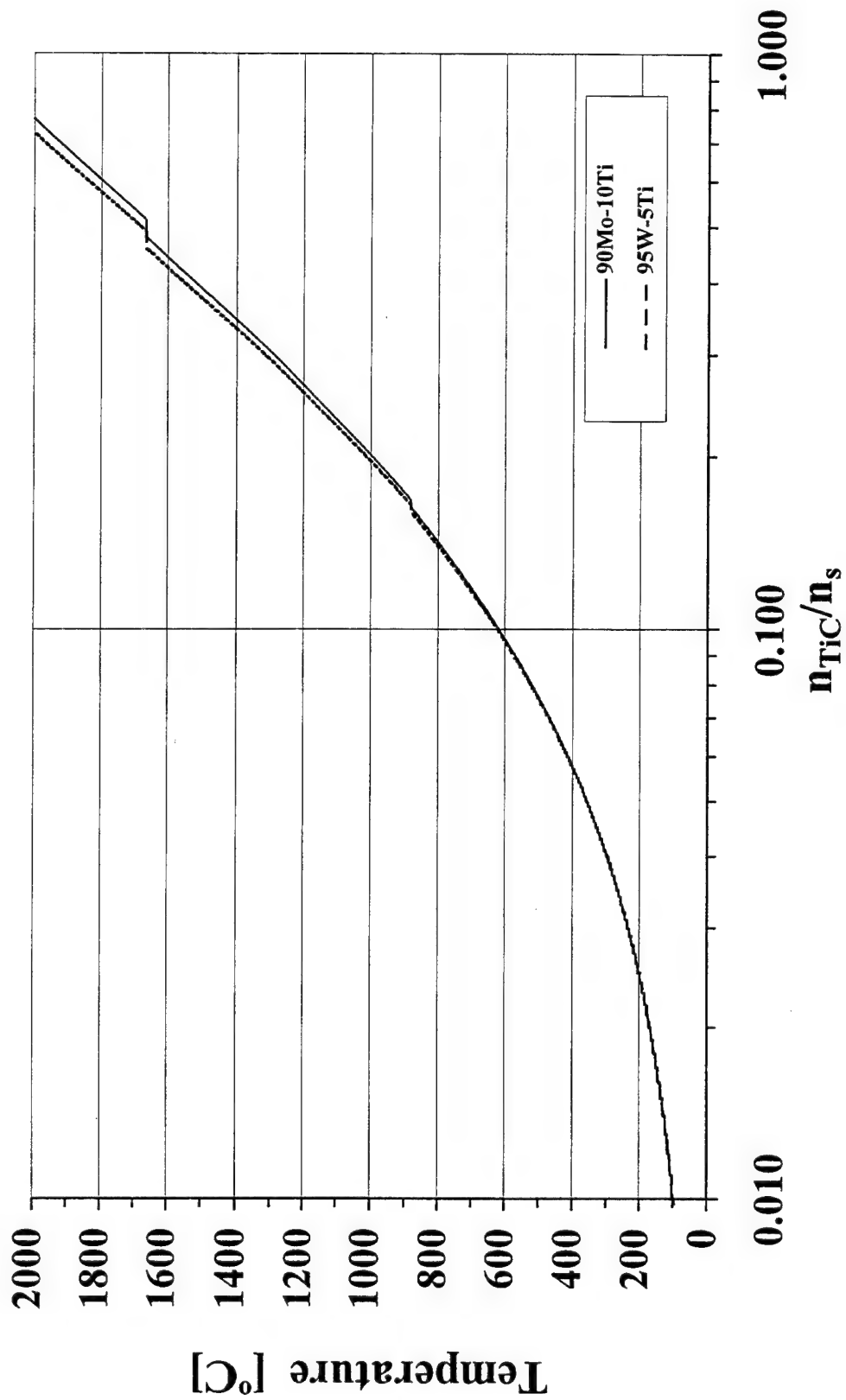
12

Figure 6. Adiabatic Heat Requirements for the 90Mo-10Ti and 95W-5Ti Samples and TiC Furnace.

13

The discrepancy between the experimentally determined $n_{TiC}{:}n_s$ value and that determined from the adiabatic heat balance indicates that the steel fixture absorbs a considerable fraction of heat generated by the TiC reaction. Based on the calculation and the experimentally obtained $n_{TiC}{:}n_s$ values, it may be surmised that about 90% of the SHS heat is lost to the surrounding steel medium.

Differences in the rate of temperature change in the powder bed are primarily influenced by kinetic factors such as the thermal diffusivity of the powder mixture. In Figure 7, a plot of the thermal diffusivity ratio, a_{Mo}/a_W, implies that over the temperature range of interest, Mo has a lower thermal diffusivity than W [18]. See Appendix D for the raw data. Therefore, it is expected that the thermal diffusivity of the Mo+Ti mixture will also be less. With a lower thermal diffusivity, the rate of change of the temperature in the Mo+Ti bed would be expected to be more sluggish.

3.2 CSA-HEC Experimental Results. The pure metal and alloy compositions considered, with the corresponding c:m, $n_{TiC}{:}n_s$, percent theoretical density (% TD), and microhardness, are listed in Table 1. In previous experiments [5], a c:m value of about 1.9 was found to produce samples with optimum (i.e., highest density without excessive cracking) results. After compaction, the CSA-HEC sample billets had a diameter of about 50 mm and an average thickness of 10 mm. The disk-shaped samples could be divided into an inner core and a periphery. Typically, the core comprised a disk with a diameter of about 35–40 mm, while the periphery comprised the outer 10- to 15-mm annulus of the billet. The periphery could be further divided into a 5-mm-wide outer edge and an intermediate transitional region. While the inner core was relatively free of cracks, the outer zone often contained planar and conical cracks.

As seen in Table 1, both of the alloys were consolidated to about 99% TD. In contrast, the densities of the pure metal samples were considerably lower. Mo was consolidated to 97.7% TD, W to 96.6% TD, and Ti to 95.6% TD.

Table 2 summarizes the XRD results for the precursor powders and the CSA-HEC samples. Baseline measurements of the lattice parameters of the precursor powders are in agreement with nominal values for Mo, W, and Ti. A c_0/a_0 of 1.586 ±0.011, obtained for Ti, is also within accepted

14
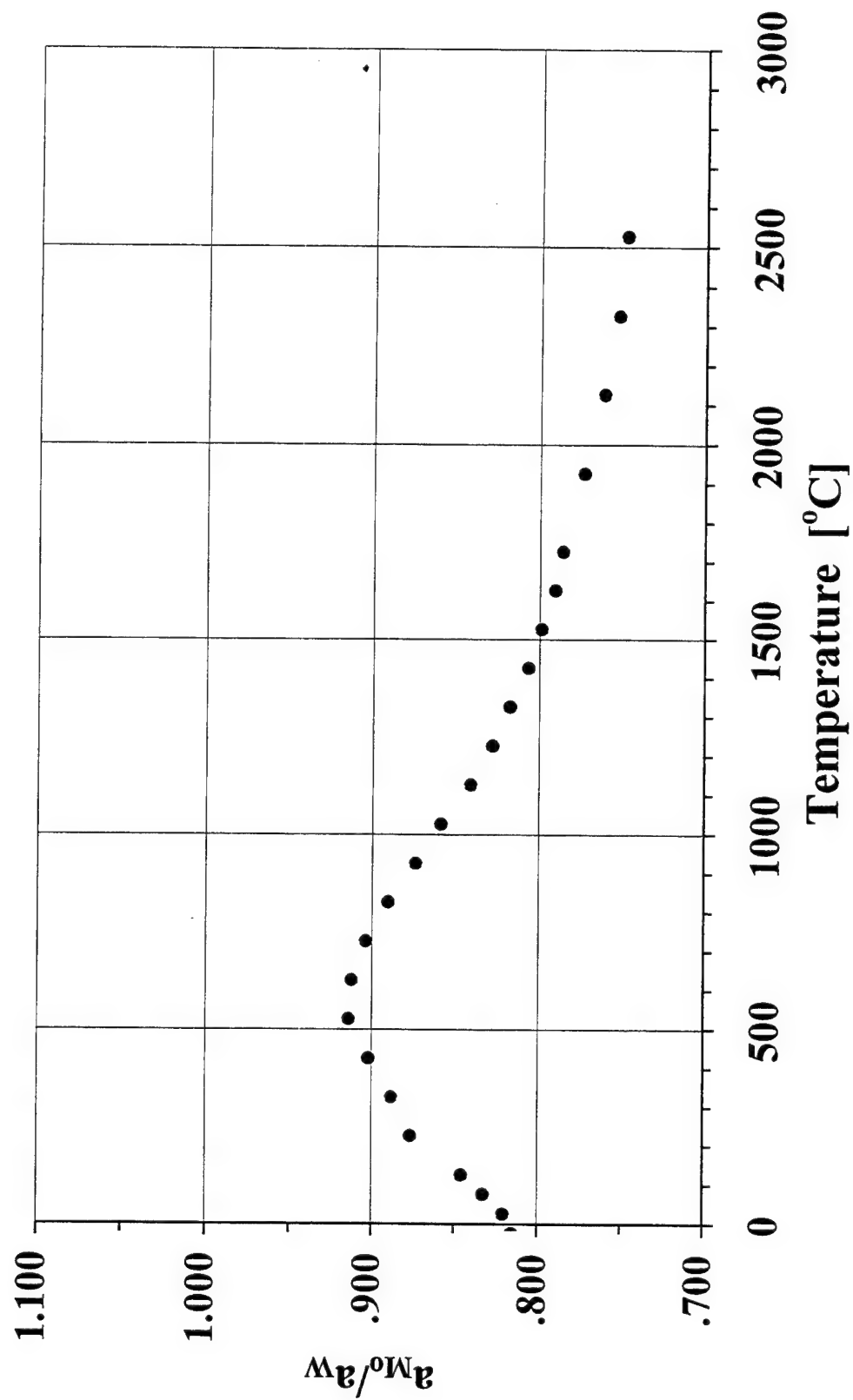
Figure 7. Ratio of the Thermal Diffusivity of Mo and W. From Touloukian [18].

15

Table 1. Description of the CSA-HEC Samples

Sample (Weight-Percent)	c:m	n_{TiC}/n_s	TD (g/cm^3)	Density (% TD)	Microhardness (GPa)	
					400 gf	100 gf
Unalloyed Metals						
W	1.72	6.12	19.25	96.6	3.8	4.1
Mo	2.19	6.09	10.22	97.7	2.4	2.6
Ti	1.70	5.60	4.51	95.6	1.9	2.0
Alloys						
95W-5Ti	1.98	6.23	16.55	98.9	5.1	5.1
90Mo-10Ti	2.09	5.77	9.07	99.1	2.9	3.7

Table 2. Lattice Parameters of the Precursors and CSA-HEC Samples

Sample (Weight-Percent)	Lattice Parameter	
	a_0	c_0
Precursor Powders		
Mo	0.31421 ±0.00002	n/a
W	0.31599 ±0.00007	n/a
Ti	0.2944 ±0.0002	0.4668 ±0.0032
Unalloyed Metals - Core Region		
Mo	0.31445 ±0.00004	n/a
W	0.31652 ±0.00004	n/a
Ti	0.29496 ±0.00007	0.46861 ±0.00002
Alloys - Core Region		
Mo in 90Mo-10Ti	0.31443 ±0.00004	n/a
W in 95W-5Ti	0.31640 ±0.00004	n/a
Unalloyed Metals - Edge Region		
Mo	0.31447 ±0.00004	n/a
W	0.31640 ±0.00004	n/a
Ti	0.29509 ±0.00007	0.46260 ±0.00003
Alloys - Edge Region		
Mo in 90Mo-10Ti	0.31444 ±0.00004	n/a
W in 95W-5Ti	0.31649 ±0.00004	n/a

norms. The nominal lattice parameter, a_0, is 0.31468 nm for Mo, and 0.31652 nm for W. For Ti, the nominal lattice parameter values are 0.29503 nm for a_0, 0.46831 nm for c_0 [19], and 1.5873 for c_0/a_0. A slight 0.1–0.3% deviation between the measured and nominal values is expected from fine, unannealed, polycrystalline particles.

Figures 8–11 display the XRD scans of the CSA-HEC samples. Results in Figures 8 and 9 from the core regions of the samples are discussed first, followed by results from the edge regions in Figures 10 and 11. X-ray diffraction scans collected from the unalloyed metal cores are shown in Figure 8. For Mo in Figure 8(a), the scan shows only Mo peaks. For W in Figure 8(b), the scan shows only W peaks. The lattice parameter reveals that the relaxation of W is greater than that of Mo. For the Ti sample in Figure 8(c), the scan shows only α-Ti peaks. The small shift in lattice parameters for Mo, W, and Ti reveals, that during the CSA-HEC process, the crystal lattices became slightly relaxed.

X-ray diffraction scans in Figure 9 show that the alloy core has a two-phase structure. In Figure 9(a), the diffraction peaks corresponding to Mo are clearly seen. Likewise, in Figure 9(b), the diffraction peaks for W can be noticed. The relaxation of the Mo phase in the 90Mo-10Ti alloy is unchanged from that in the unalloyed metal. The degree of relaxation of W in the 95W-5Ti alloy is slightly reduced from that in the pure metal. The second phase in each alloy appears as a shoulder (with an inflection point) on the low-angle side of each main peak. In the 90Mo-10Ti alloy, the shoulders are more magnified and also much wider, extending to lower angles. Additionally, unlike the 95W-5Ti alloy, a few distinct peaks appear on the shoulders.

Figure 10 displays the XRD scans from the edge regions of the unalloyed metal samples. Shown in Figure 10(a), the shape and positions of the primary Mo peaks from the edge of the unalloyed metal sample appear to be the same as those from the core. The similarities of the scans are supported by lattice parameter data for Mo, which indicate little difference between the extent of relaxation of the two regions. The edge scan for W in Figure 10(b) is virtually identical to that of the core, but the region is less relaxed than the core region. A larger distortion is observed for Ti, which is reflected in a shift in the peak positions, as well as in the lattice parameter data.

17

Figure 8. X-ray Diffractograms of the Core Regions of the Unalloyed Metals: (a) Mo, (b) W, and (c) Ti.

Figure 8. X-ray Diffractograms of the Core Regions of the Unalloyed Metals: (a) Mo, (b) W, and (c) Ti (Continued).

(b)

19

Figure 8. X-ray Diffractograms of the Core Regions of the Unalloyed Metals: (a) Mo, (b) W, and (c) Ti (Continued).

(c)

20

Figure 9. X-ray Diffractograms of the Core Regions of the Alloy Samples: (a) 90Mo-10Ti and (b) 95W-5Ti.

(a)

21

Figure 9. X-ray Diffractograms of the Core Regions of the Alloy Samples: (a) 90Mo-10Ti and (b) 95W-5Ti (Continued).

Figure 10. X-ray Diffractograms of the Edge Regions of the Unalloyed Metals: (a) Mo, (b) W, and (c) Ti.

(a)

Figure 10. X-ray Diffractograms of the Edge Regions of the Unalloyed Metals: (a) Mo, (b) W, and (c) Ti (Continued).
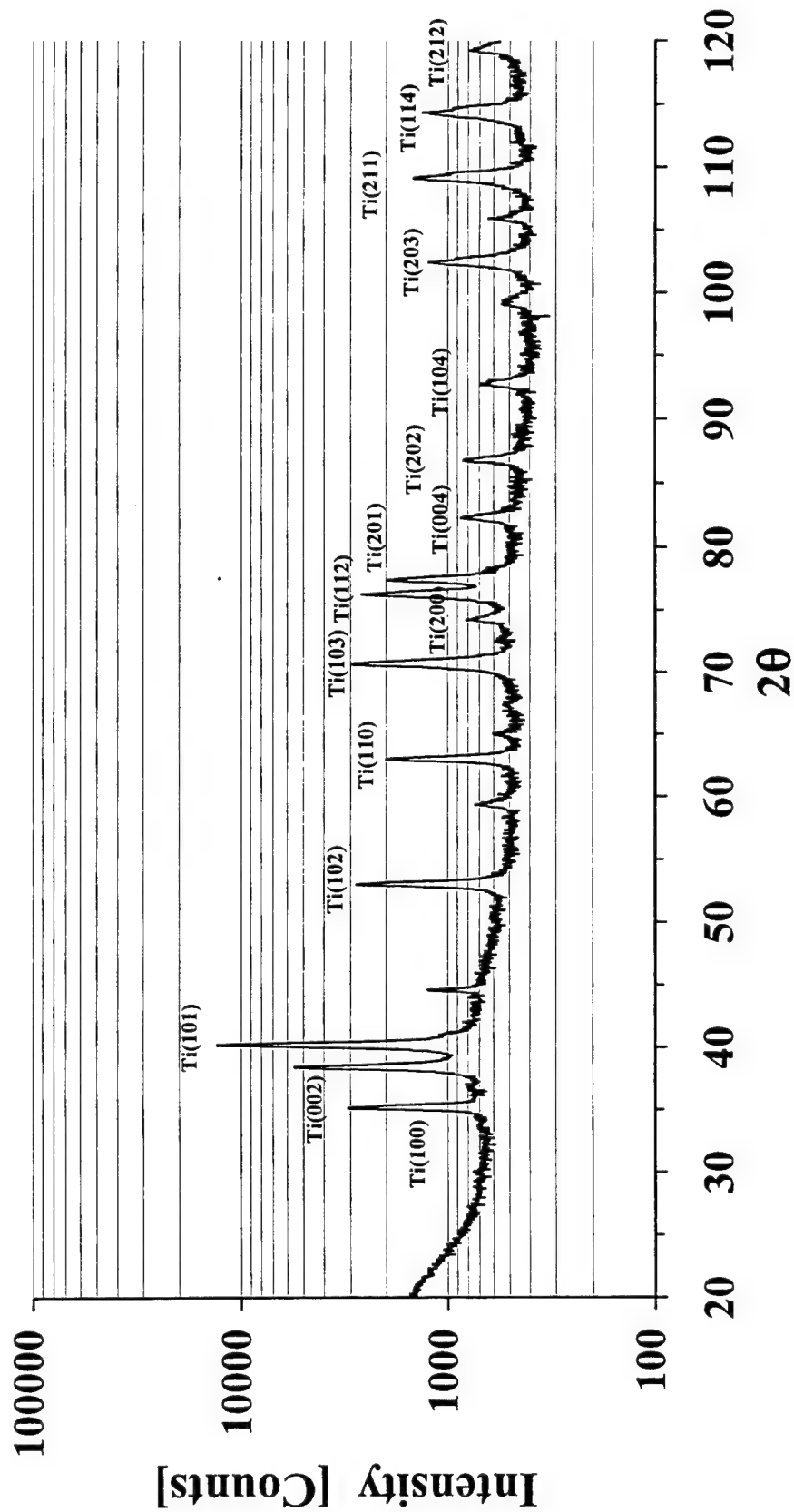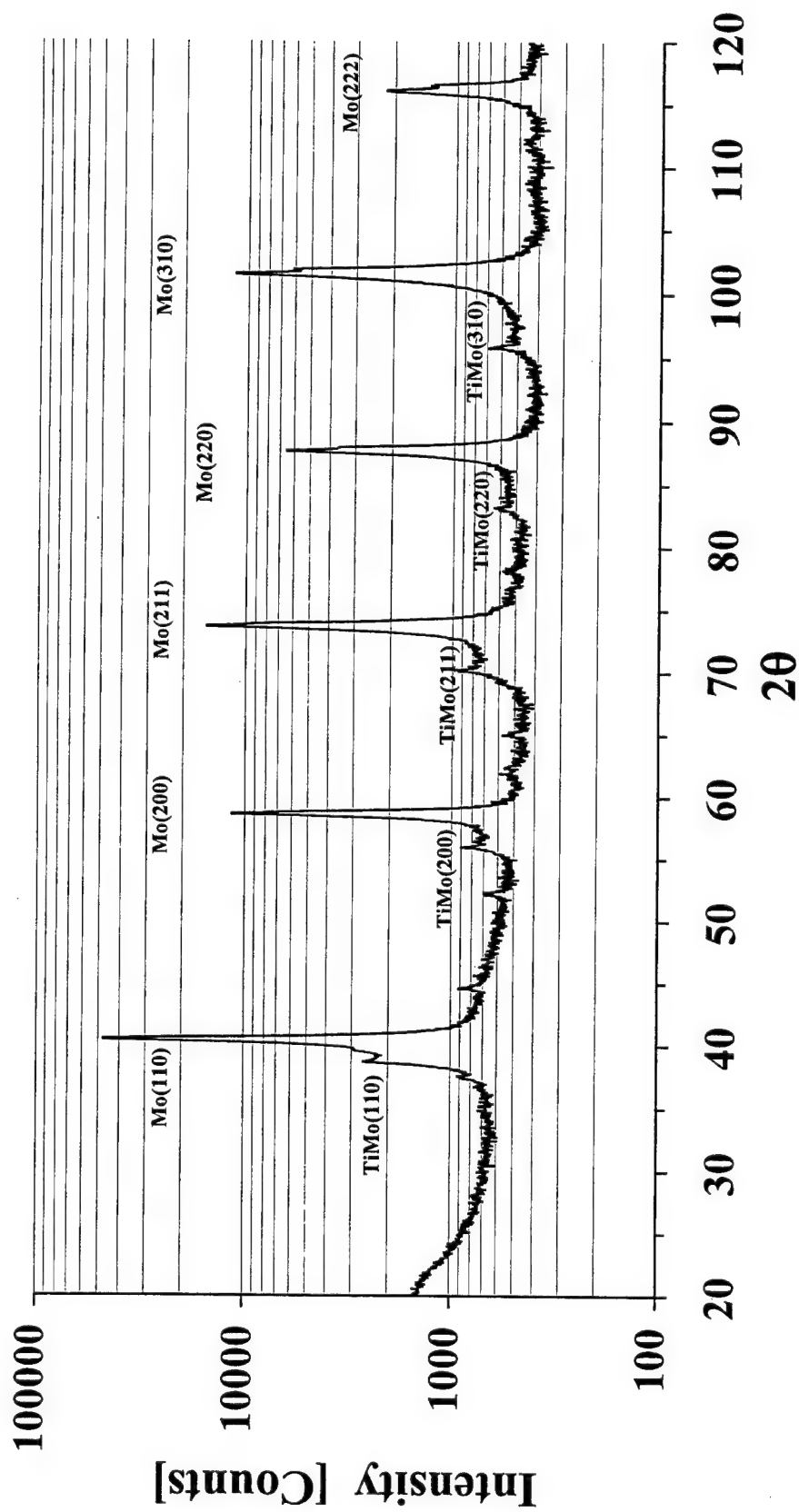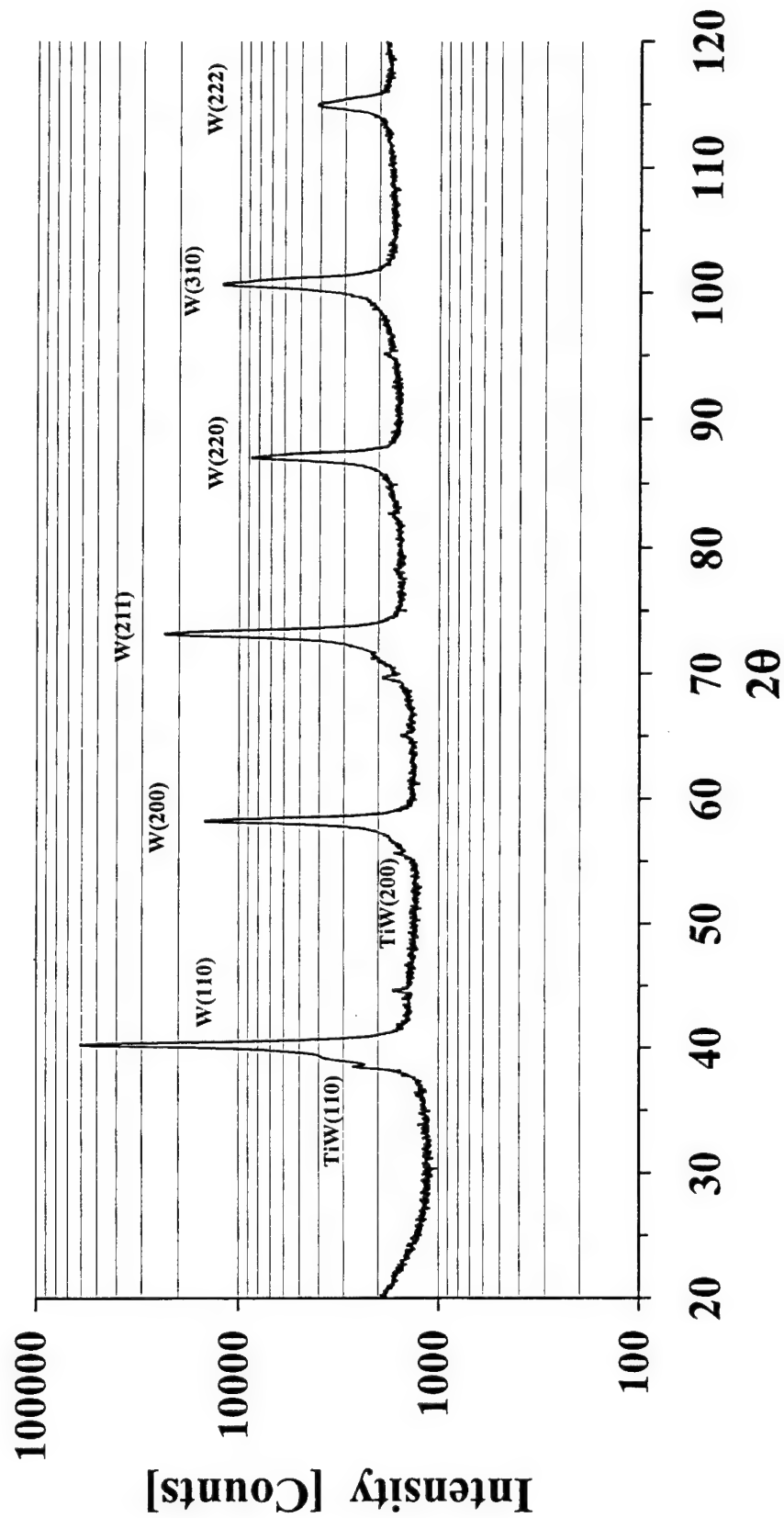
(b)

24

Figure 10. X-ray Diffractograms of the Edge Regions of the Unalloyed Metals: (a) Mo, (b) W, and (c) Ti (Continued).
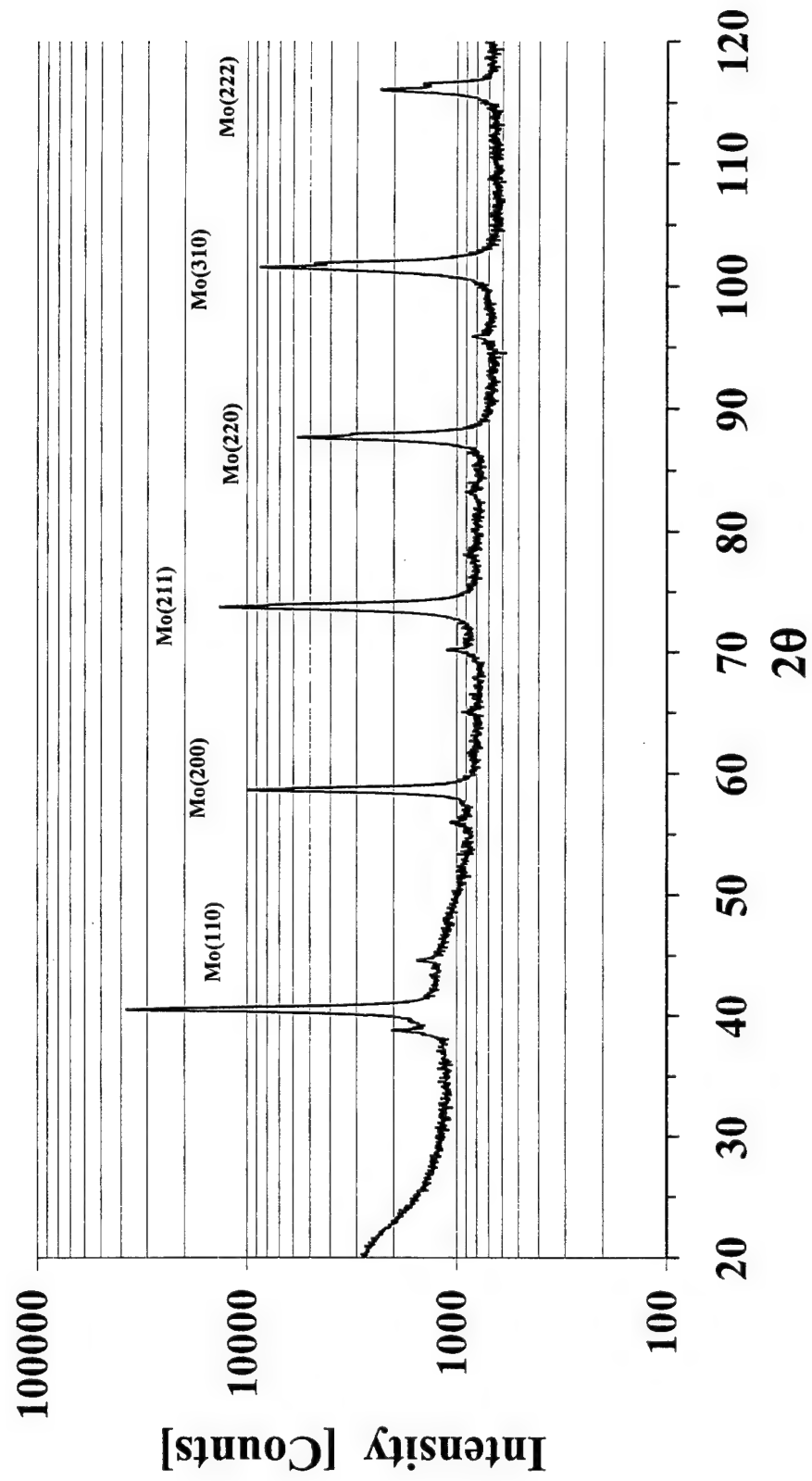
(c)

25

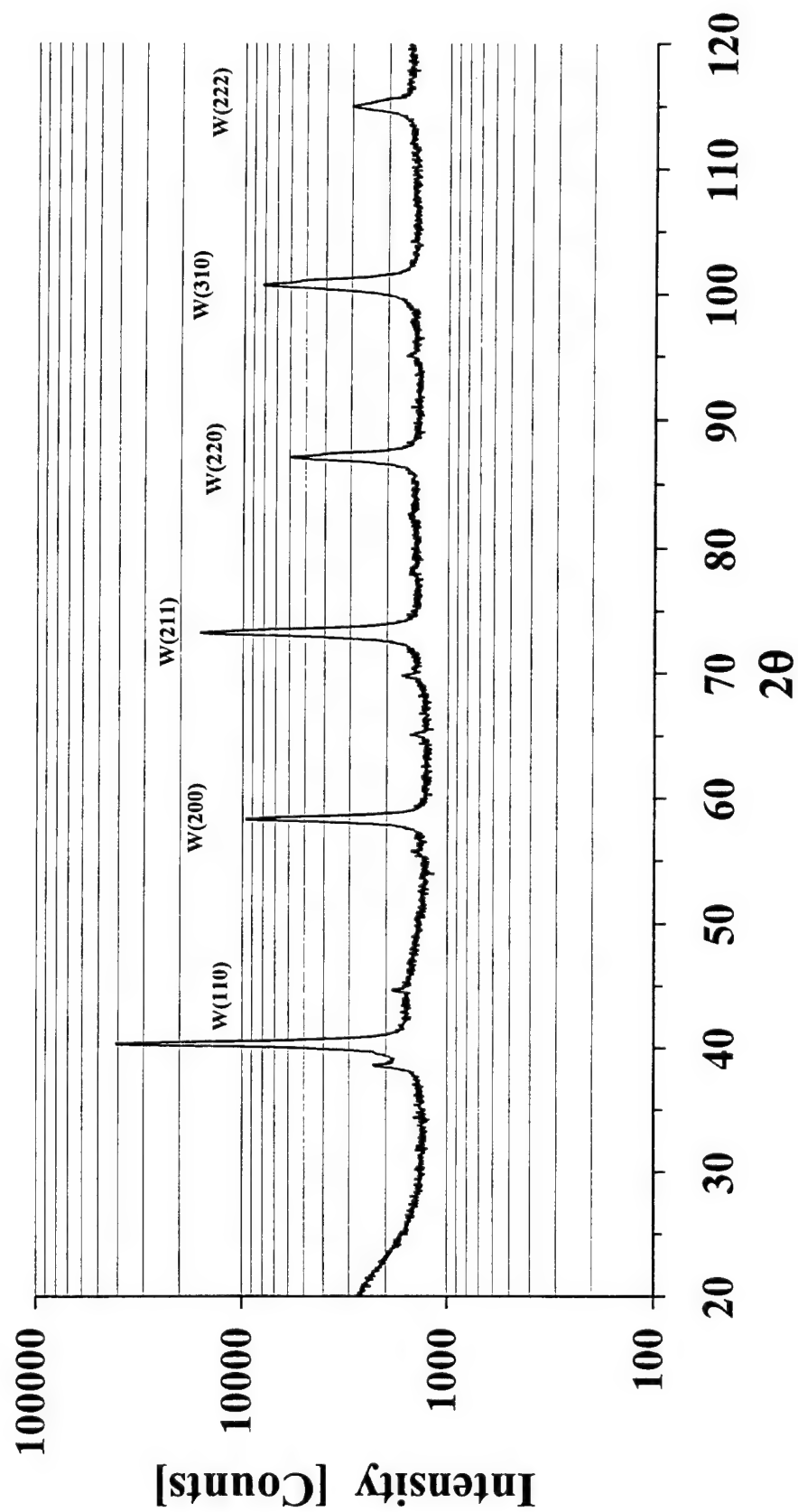Figure 11. X-ray Diffractograms of the Edge Regions of the Alloy Samples: (a) 90Mo-10Ti and (b) 95W-5Ti.

(a)

26

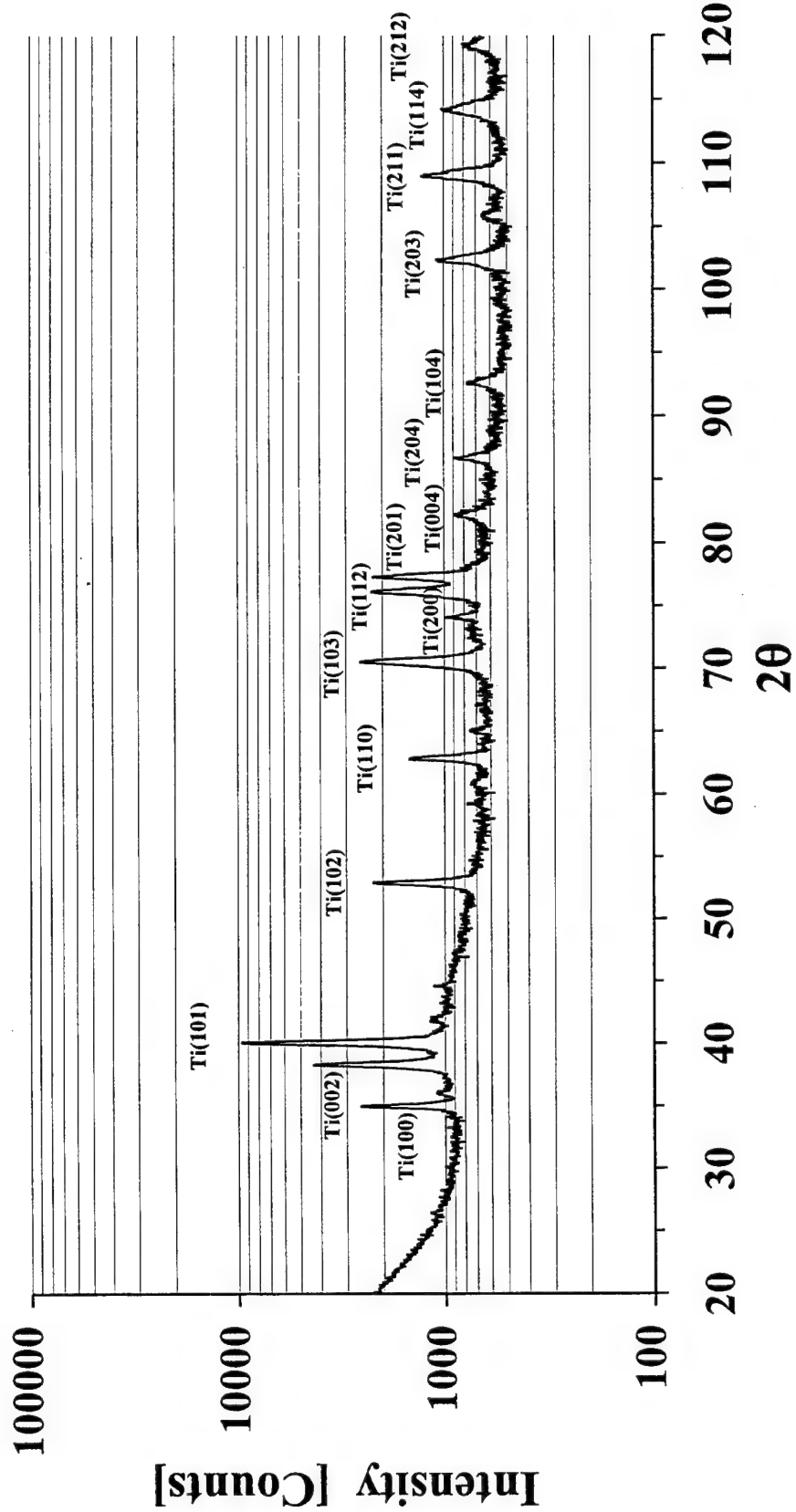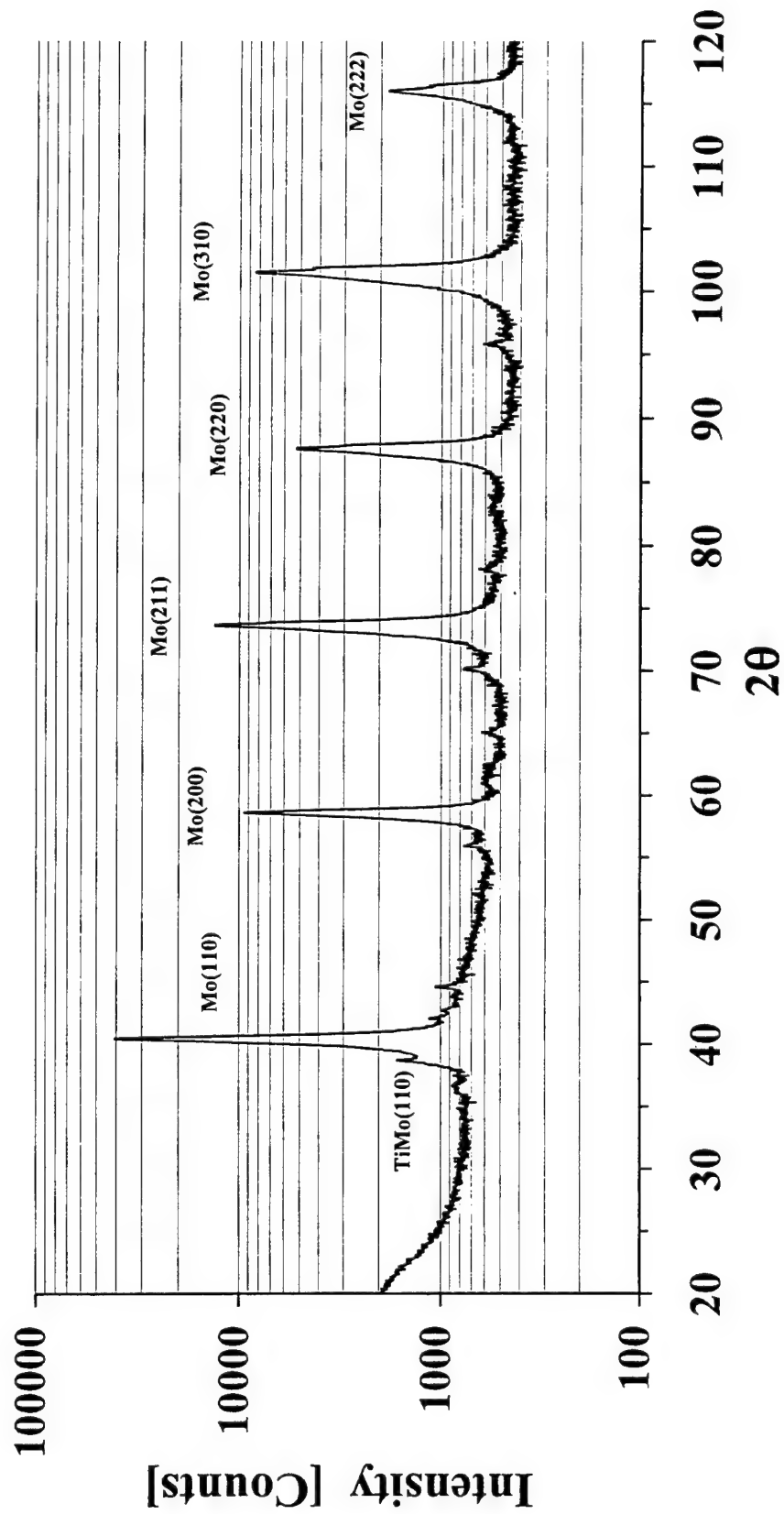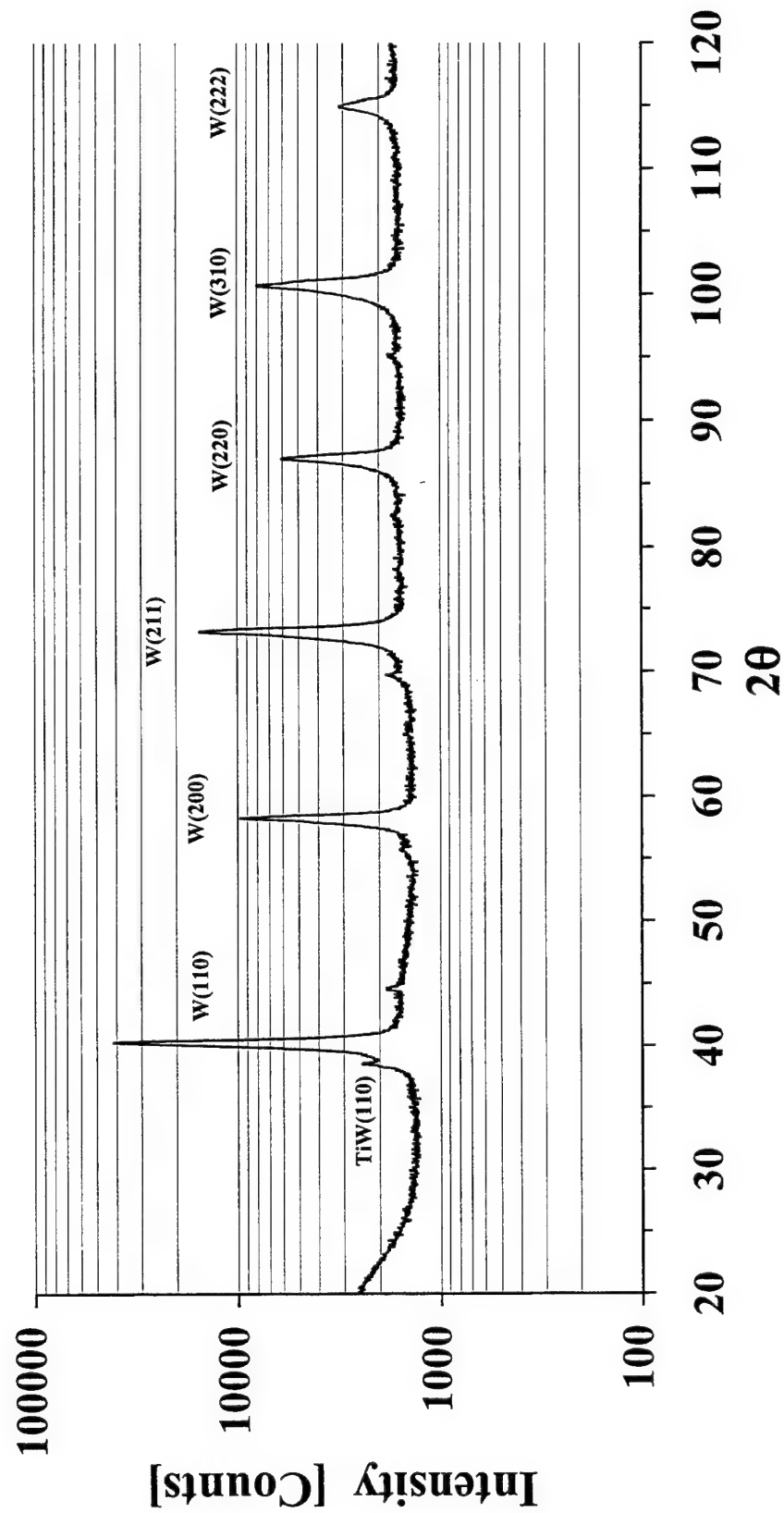Figure 11. X-ray Diffractograms of the Edge Regions of the Alloy Samples: (a) 90Mo-10Ti and (b) 95W-5Ti (Continued).

27

X-ray diffraction results from the edge regions of the alloyed samples are shown in Figure 11. As expected, the degree of relaxation of the primary peaks in the alloys is similar to that of the unalloyed metals. The lattice parameters from the edge region are not much different from those that were seen from the core region. However, the second phase profiles of the edge region scans appear to be different. Such shifts reflect a compositional change between the core and edge regions of the alloy samples. A careful examination of the Mo peaks in Figure 11(a) reveals that the peaks have broader low-angle sides, and their shoulders, unlike those seen in Figure 9(a), are somewhat smaller. Results for the 95W-5Ti alloy, shown in Figure 11(b), are equally subtle. In the edge region scan, the W peak shape has shifted from having a shoulder to a more gradual, monotonic decline extending to lower angles.

Orthogonal cross sections of the alloy samples (with respect to the compaction axis) revealed that the distribution of the primary and secondary phases was isotropic in the basal plane; however, both phases were transversely elongated in the axial plane. This orientation effect arose from the uniaxial collapse of the initially isotropic powder bed. The distortion was not observed in the pure metals. Axial cross sections from the core of the sample billets are illustrated in Figure 12. The 90Mo-10Ti alloy is shown in Figure 12(a), the 95W-5Ti alloy in Figure 12(b), the W in Figure 12(c), the Mo in Figure 12(d), and the Ti in Figure 12(e).

Observation of the 90Mo-10Ti alloy revealed that the Mo grain aggregates (light gray) are interconnected, surrounding mostly isolated Ti-rich matrix regions (medium to dark gray). The Mo grains have a size of 10–30 µm. The dimensions of the Ti-rich matrix regions correspond to those of the Ti precursor. Energy dispersive x-ray spectroscopy of the sample indicates that, in all cases, the Mo in the aggregates is mostly pure. As evident in Figure 12(a), the Ti-rich matrix phase is segregated and nonuniform (i.e., cored). The composition of the medium gray areas ranges from 40Mo-60Ti to 25Mo-75Ti. In contrast, the composition of the dark gray areas is mostly pure Ti. The low-angle shoulders, noted in the XRD scans, correspond to the Ti-rich β-Ti/Mo solid solution. The increased width and height of the shoulders correspond to the observed nonuniformity in composition. Finally, some of the distinct peaks (i.e., at 2Θ of 34.9°, 38.7°, 52.2°, 63°, and 70.1°) on the shoulders are most likely associated with the mostly pure Ti regions.
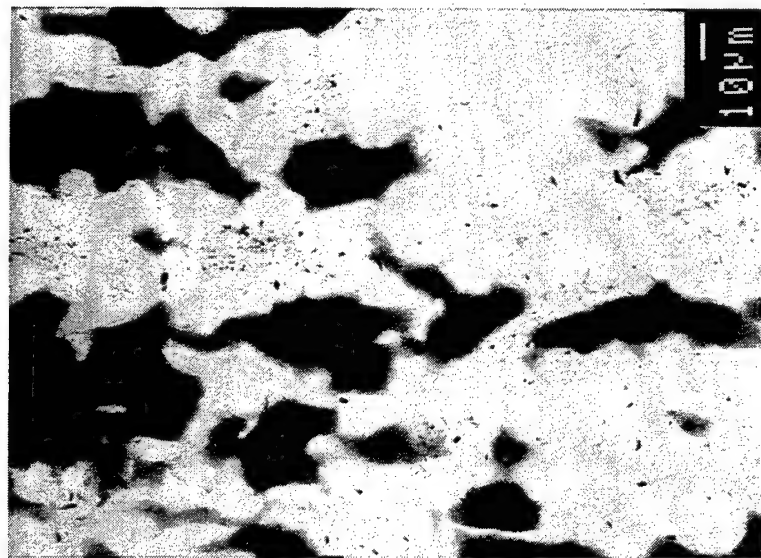
(a)
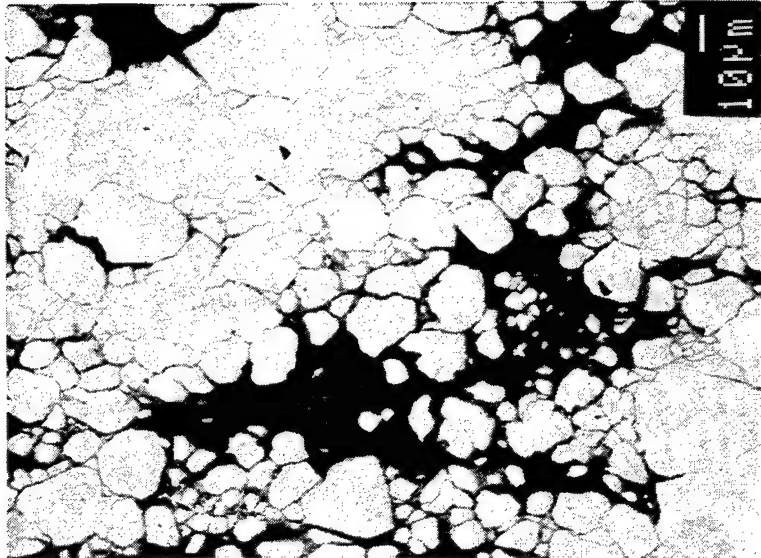
(b)

Figure 12. Scanning Electron Micrographs of the Core Region of the CSA-HEC Samples: Alloys in (a) 90Mo-10Ti and (b) 95W-5Ti and Unalloyed Metals in (c) Mo, (d) W, and (e) Ti.

29

Figure 12. Scanning Electron Micrographs of the Core Region of the CSA-HEC Samples: Alloys in (a) 90Mo-10Ti and (b) 95W-5Ti and Unalloyed Metals in (c) Mo, (d) W, and (e) Ti (Continued).
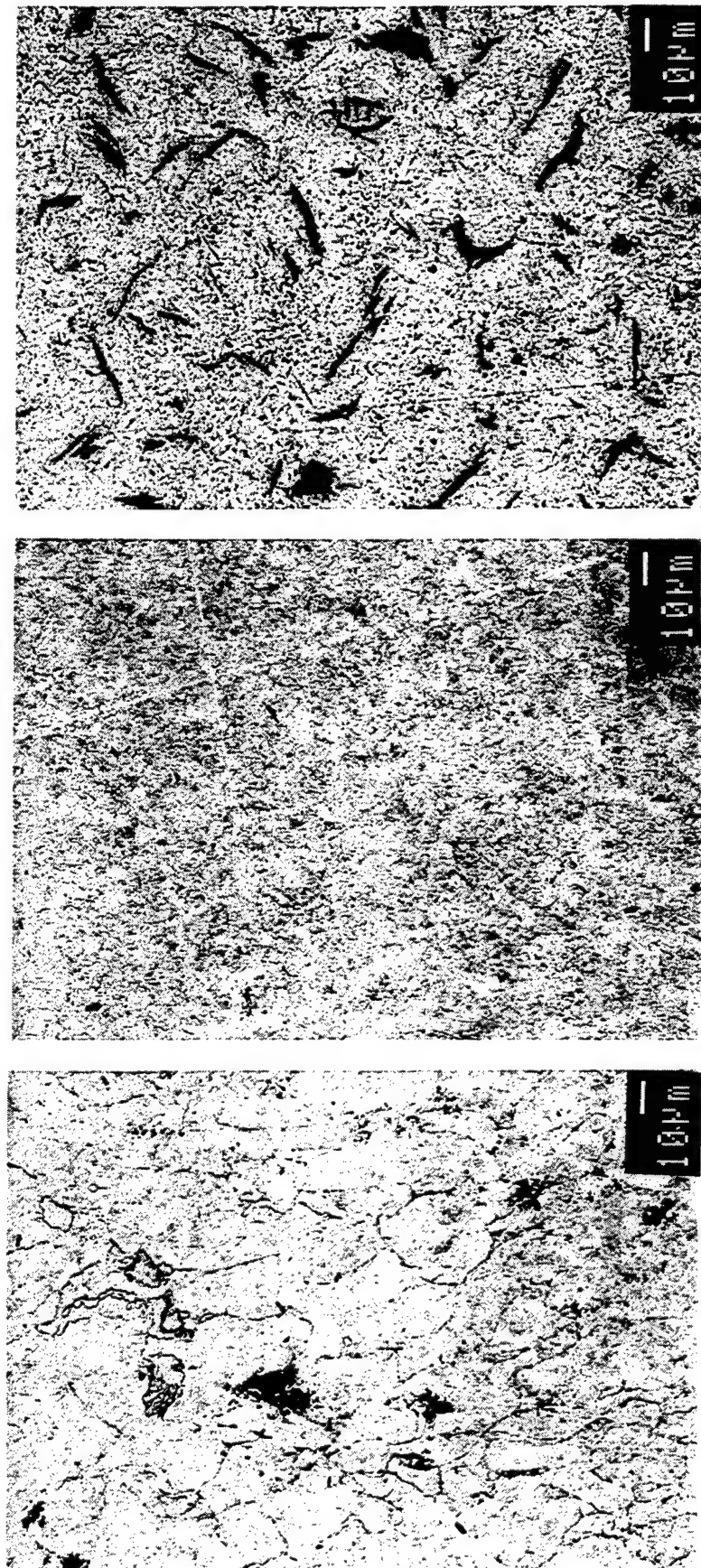
(c)   (d)   (e)

30

The structure of the 95W-5Ti alloy is dissimilar from the 90Mo-10Ti alloy. The core region reveals loose W grain aggregates (light gray) bounded by a partially connected Ti-rich matrix (dark gray). The partial discontinuity of the matrix comes from the particle size difference of the precursors, the relative melting points, and the temperature before and at the time of compaction. The W grains have retained their original size of 10 to 20 µm. The dimensions of the Ti-rich areas, likewise, correspond to the size of the Ti precursor. Though not apparent in Figure 12(b), the matrix phase contains an equiaxed grain structure with a size of 5 to 10 µm. Semiquantitative EDS indicates that the W in the aggregates is nearly pure, and the fairly uniform Ti-rich phase has a composition of about 55W-45Ti. Similar to the 90Mo-10Ti alloy, the second phase observed is the Ti-rich solid solution of β-Ti/W.

In Figure 12(c), the inner core of the unalloyed Mo reveals a generally equiaxed grain structure. Although the morphology of the Mo powder is generally retained with trapped porosity primarily along the grain boundaries, there is a slight orientation effect (i.e., compressive deformation of the grains along the compaction axis) in this sample. Also note, the grains are separated by a thin grain boundary phase.

SEM of an etched cross section from the unalloyed W's inner core reveals an equiaxed grain structure. Again, the preferential orientation seen in the alloys is absent. As shown in Figure 12(d), the precursor W powder morphology is retained with some fine porosity remaining along grain boundaries and junctions. As is apparent from the SEM micrograph and taking note of the extremely high melting point of W, it may be concluded that the n_{TiC}:n_s used generated insufficient temperatures to melt the W in the interior of the powder bed.

The SEM micrograph of the unalloyed Ti (Figure 12(e)) shows randomly distributed, heavily deformed, elongated grains with a secondary darker phase between grains. From the appearance of the grains and the absence of excessive grain growth, it may be concluded that in the interior the temperature was sufficiently high for compaction but did not exceed T_m of Ti. The grain boundary phase is most likely attributed to the titanium dioxide (TiO_2) surface film stripped away during consolidation.

31

The SEM micrographs shown in Figures 13(a) and (b) of the outer 10 to 15 mm periphery of both alloys revealed significant changes in their respective substructures from those seen in the core regions. Both alloys are similar, containing Mo or W grain remnants (light gray) surrounded by a continuous Mo- or W-rich solid solution (medium gray). The shift from rounded to polyhedral morphology of the Mo or W grains clearly reflects the presence of extreme temperatures. Energy dispersive spectroscopy indicated more extensive dissolution and intermixing between components as about 90Mo-10Ti and 90W-10Ti were measured. The Mo-Ti or W-Ti solid solution also contains isolated regions (dark gray to black) that are mostly Ti, 5Mo-95Ti, or 2W-98Ti.

Examination of the metals (Figures 13(c), (d), and (e)) confirmed the considerably higher temperatures in these regions as well. Grain growth was most noticeable in Ti. Furthermore, Ti grains exhibited much more deformation and elongation than observed at the core of the billet. For Mo, no notable grain growth occurred; however, the number of closed pores was reduced. No grain growth occurred in W.

A plausible explanation for the lower percent theoretical density (% TD) of the unalloyed metals compared to the alloys may be offered by considering the peak temperature, T_p, during the preheating phase and T_m. At the core, the peak temperature, reached at the time of consolidation, is $T_{pc} = 1,550°$ C. The T_{pc}/T_m ratio at the core is 0.45 for W, 0.59 for Mo, and 0.93 for Ti. It is estimated that at the edge, a peak temperature of about $T_{pe} = 2,000°$ C is reached during preheating. At the edge region, therefore, the T_{pe}/T_m ratio is 0.58 for W, 0.76 for Mo, and 1.20 for Ti.

In Mo and W, the $n_{TiC}:n_s$ value was insufficient to elevate the powder temperatures high enough to cause thermal softening. No structural changes occurred (i.e., those that would indicate melting) at the edge of the Mo or W powder bed. As was observed in Figure 12, the effect of higher temperatures during preheating was reflected in grain growth only. Therefore, it may be concluded that while the differences between core and edge temperatures during the preheating phase are major, its effect on densification was minor. The impact of this difference is further reduced, as at the time of consolidation, the edge region cools and its temperature is the same as that of the core. Consequently, it may be surmised that these powders remained too stiff to be adequately densified.

32
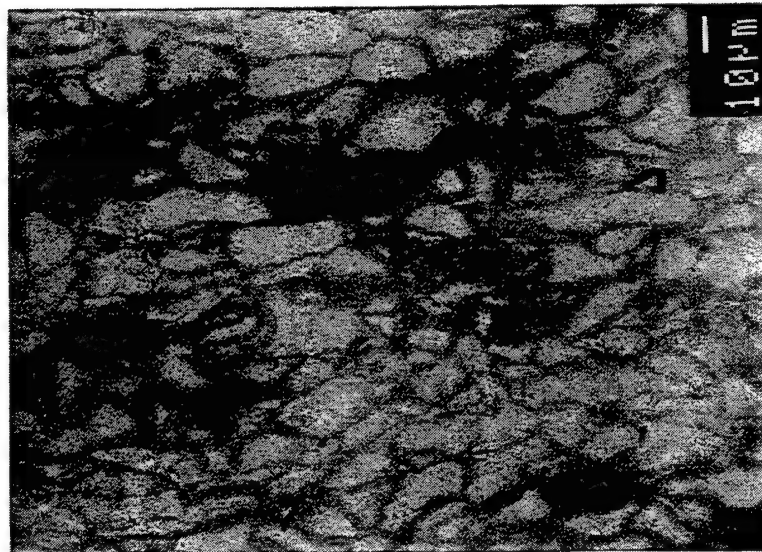
(a)
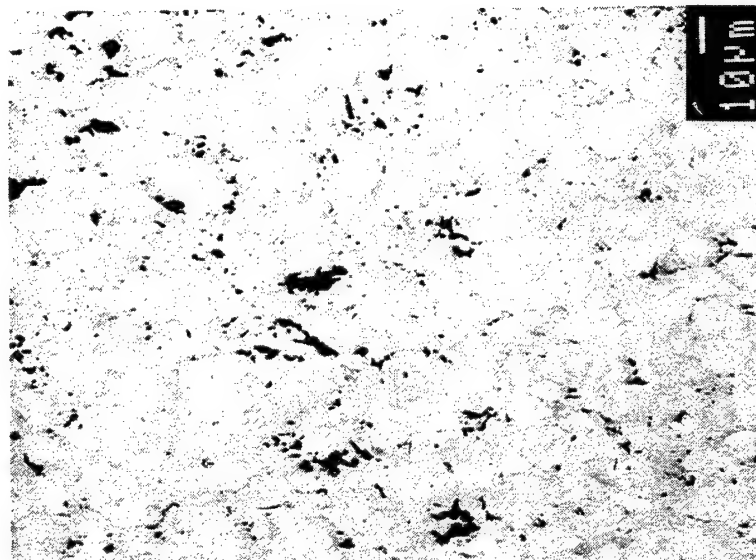
(b)

Figure 13. Scanning Electron Micrographs of the Edge Region of the CSA-HEC Samples: Alloys in (a) 90Mo-10Ti and (b) 95W-5Ti and Unalloyed Metals in (c) Mo, (d) W, and (e) Ti.

33

Figure 13. Scanning Electron Micrographs of the Edge Region of the CSA-HEC Samples: Alloys in (a) 90Mo-10Ti and (b) 95W-5Ti and Unalloyed Metals in (c) Mo, (d) W, and (e) Ti (Continued).

34

For Ti, the $n_{TiC}:n_s$ value was considerably higher, rendering the core most plastic among the metals; however, its compaction yielded the lowest % TD. Unlike Mo and W, where T_m was not exceeded, in this case, local melting at the edge occurred; as a result, the open pores connecting the interi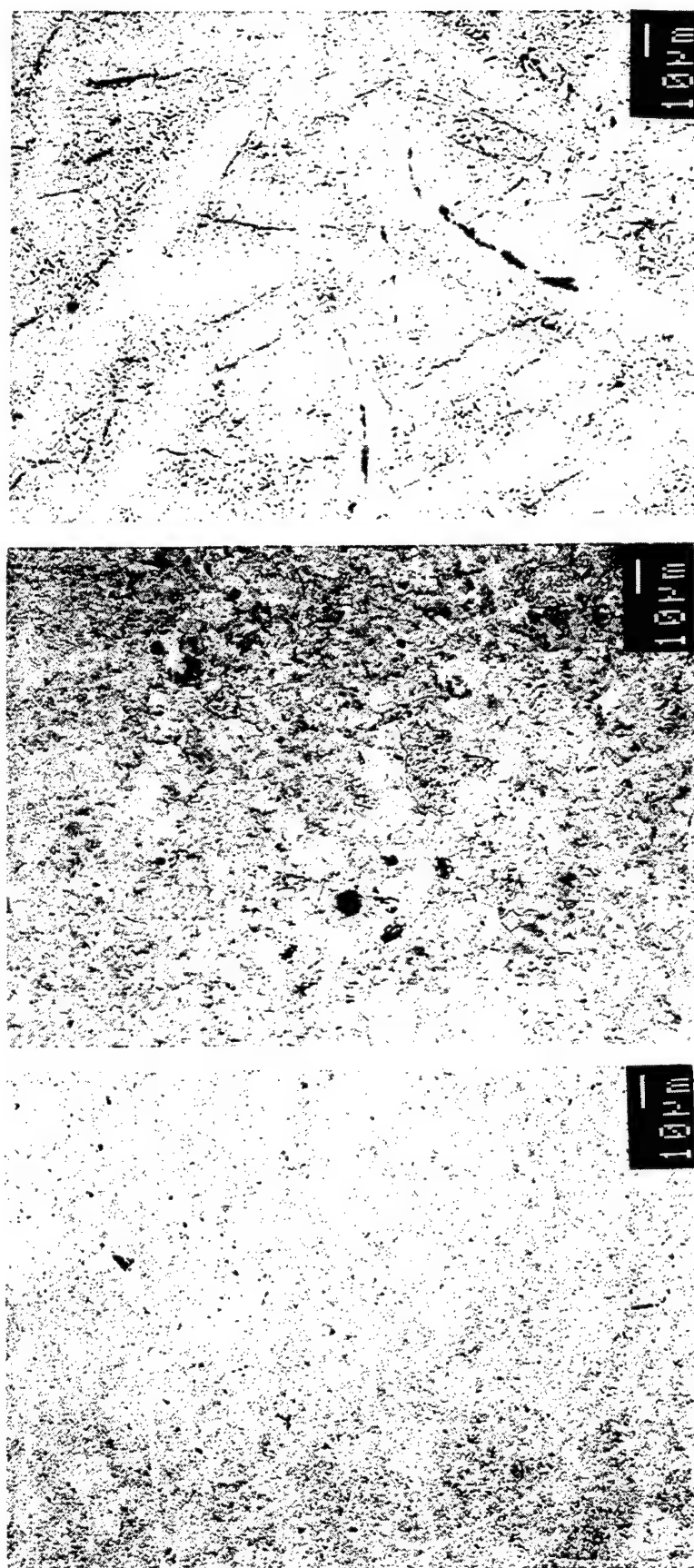or to the outer surface collapsed and were eliminated. At consolidation, this region also cooled below, but near T_m, whereby the collapsed structure was preserved. However, despite the existence of a highly plastic state, the lack of exit routes in the powder bed prevented venting and complete closure of the interior porosity.

The evolution of the alloy microstructure is complicated by the presence of the matrix phase. The added difficulty derives from the intermixing of the constituents at elevated temperatures. In the 95W-5Ti alloy, because of the moderately fast diffusion of W in Ti [20] and the fact that the sample is consolidated at a sufficiently long time delay, it was expected that the composition of the β-Ti/W solid solution would equilibrate during preheating. The concentration gradient introduced by the solid-state dissolution of the outer layer of the W grains in Ti would be quickly reduced by rapid diffusion. In the absence of a composition gradient (i.e., that introduced by slow diffusion), the rate-controlling step of the process is the dissolution of W during preheating. The structural features of the matrix in the 95W-5Ti alloy are in good agreement with this assessment.

In the 90Mo-10Ti alloy, the matrix does not have a uniform composition, but is cored. Based on the thermodynamics of the CSA-HEC system, the higher rate of diffusion of Mo in Ti (about three times that of W in Ti) and the strong similarities between the Mo-Ti and W-Ti phase diagrams ought to result in a compositionally uniform matrix similar to that found in the 95W-5Ti alloy. However, due to the lower thermal diffusivity of Mo, the nominal compaction delay time is insufficient to allow adequate equilibration of the β-Ti/Mo matrix. The more sluggish temperature rise reduces the effectiveness of preheating, and a shorter time at temperature, in turn, prevents the homogenization of the matrix composition.

It is expected that the reaction kinetics should be the same at the peripheral regions of the alloys. Due to higher local temperatures, differences between the core and edge structures ought to be manifested in more extensive intermixing between components only. However, an undesirable result

35

of the higher temperatures at the periphery is that the solid solution composition could move into or beyond the miscibility gap (see Figure 4). This, in turn, would cause the observed phase separation of the matrix phase during cooling.

Fracture surfaces from the core region of the alloy and metal billets are shown in Figure 14. Failure occurred by inter- and transgranular fracture in the 90Mo-10Ti and 95W-5Ti alloy samples. See Figures 14(a) and 14(b). In the 90Mo-10Ti sample, the Mo grains that failed by intergrain separation exhibited limited ductility (dimpling of the separated grain surfaces). Whereas, the Ti-rich areas usually failed by a characteristically brittle, transgranular cleavage. The failure mode of the 95W-5Ti alloy is similar, but less ductility is present in the W grains. In Figures 14(c) and 14(d), fracture surfaces from the unalloyed W and Mo also reveal mixed mode failure, however, the incidence of intergranular separation is much higher. This, of course, is most likely caused by the absence of a binder phase. The fracture surface in Figure 14(e) from the unalloyed Ti is more typical of ductile failure. In addition to transgranular cleavage, the relatively large Ti grains exhibit extensive dimple formation.

Sample microhardnesses primarily reflect dispersion hardening effects. As evident in Table 1, there is a notable 20–30% increase in overall hardness when Ti is added to W or Mo. This increase is caused by the formation of the Ti-rich β-Ti/W or β-Ti/Mo solid solution. With the exception of 90Mo-10Ti, the sample hardnesses are essentially load-independent. The larger deviation in the 90Mo-10Ti sample is attributed to the presence of the cored matrix. Particularly, the 100-gf hardness (i.e., 3.7) is higher due to a few points from the central Ti area of the matrix regions. The higher scatter in the data also results in a larger limit of error of 0.30 GPa. (Note, when these points are omitted, the overall hardness becomes 3.2, reducing the apparent deviation to match that of the other samples.)
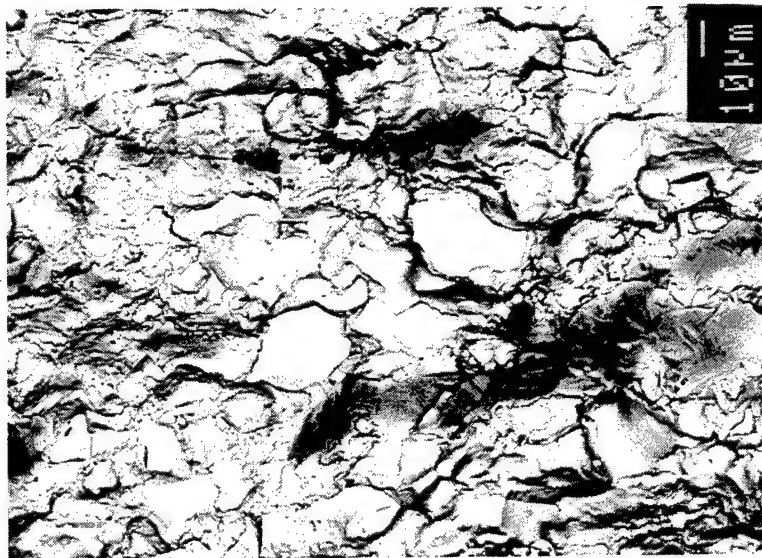
(a)
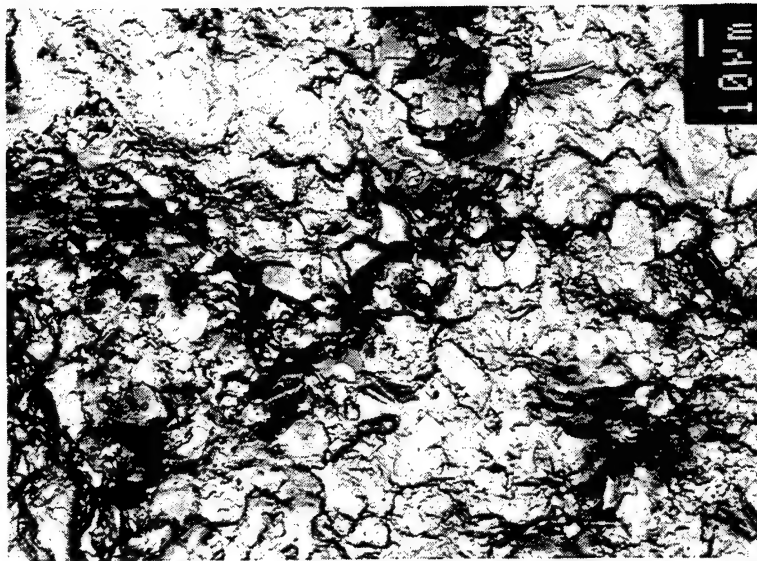
(b)

Figure 14. Scanning Electron Micrographs of Fracture Surfaces From the Core Region of the CSA-HEC Samples: Alloys in (a) 90Mo-10Ti and (b) 95W-5Ti and Unalloyed Metals in (c) Mo, (d) W, and (e) Ti.

Figure 14. Scanning Electron Micrographs of Fracture Surfaces From the Core Region of the CSA-HEC Samples: Alloys in (a) 90Mo-10Ti and (b) 95W-5Ti and Unalloyed Metals in (c) Mo, (d) W, and (e) Ti (Continued).

38

4. Conclusions

A novel CSA-HEC technique designed for the fabrication of Mo, W, Mo-Ti, and W-Ti alloys has been described. The elemental constituent powders of the billet are heated by an external Ti+C SHS reaction. In the current arrangement, the heat evolved in the SHS reaction diffuses slowly into the powder bed by conduction. The powder bed is allowed to become isothermal, and, at the time of consolidation, it is compacted to high density by the detonation of a high explosive.

The core of the W-Ti alloy billets is of high density and consists of a two-phase structure with W particles embedded in a partially continuous Ti-rich β-Ti/W solid solution matrix. The alloy is transversely oriented and has spatially dependent structural features. Hardness measurements indicate that the W-Ti alloy is affected by dispersion hardening.

Experiments with the Mo-Ti system resulted in similar overall alloy characteristics. Within the interior, unlike the matrix in the W-Ti alloy, the matrix in the Mo-Ti alloy is cored. This substructure arises from the sluggish kinetics of the preheating phase, causing the dissolution of the primary component to be nonuniform and incomplete. The coring may be reduced by internal or external modifications to the CSA-HEC fixture whereby the duration of the isothermal plateau is lengthened. Alternatively, the cored Mo-Ti alloy could be heat-treated below the monotectoid temperature to enhance or complete the solid solution formation.

While both W-Ti and Mo-Ti alloys were compacted with good results, none of the unalloyed metals compacted to full density. Results of the compaction with the unalloyed metals indicate that the absence of a low melting point secondary component (binder phase) appears to degrade the compatibility of the sample. The degree of densification reveals that there is an optimum powder stiffness, which is determined by the ratio of the temperature at consolidation and the melting point. In the CSA-HEC fixture, this ratio is about 0.7.

39

INTENTIONALLY LEFT BLANK.

5. References

1. German, R. M. *Liquid Phase Sintering*. New York: Plenum Press, 1985.

2. Magness, L. S., and T. G. Farrand. "Deformation Behavior and Its Relationship to the Penetration Performance of High-Density KE Penetrator Materials." *17th Army Science Conference Proceedings*, Durham, NC, May 1990, Army Science Board, Washington, DC, vol. 2, pp. 149–164, 1990.

3. Massalski, T. B., H. Okamoto, P. R. Subramanian, and L. Kacprzak, eds. *Binary Alloy Phase Diagrams*. New York: William W. Scott, pub., 1990.

4. Bose, A., and R. J. Dowding, eds. *Tungsten and Refractory Metals 2*. Metal Powder Industries Federation, pp. 219–234, Princeton, NJ, 1995.

5. Kecskes, L. J., and I. W. Hall. "Hot Explosive Consolidation of W-Ti Alloys." ARL-TR-669, U.S. Army Research Laboratory, Aberdeen Proving Ground, MD, January 1995.

6. A. Cross. "Try Hot Explosive-Compaction for Sintered Powder Products." *Iron Age*, vol. 184, no. 26, pp. 48–50, December 1959.

7. Gorobtsov, V. G., and O. V. Roman. "Hot Explosive Pressing of Powders." *Int. J. Powder Metall.*, vol. 11, no. 1, pp. 55–60, January 1975.

8. Bhalla, A. K. "Hot Explosive Compaction of Metal Powders." *Trans. Powder Metall. Assoc. India*, vol. 7, no. 9, pp. 1–8, September 1980.

9. Wang, S. L., M. A. Meyers, and A. Szeket. "Warm Shock Consolidation of IN718 Powder." *J. Mater. Sci.*, vol. 23, no. 5, pp. 1786–1804, May 1988.

10. Ferreira, A., M. A. Meyers, N. N. Thadhani, S. N. Chang, and J. R. Kough. "Dynamic Compaction of Titanium Aluminides by Explosively Generated Shock Waves: Experimental and Material Systems." *Metall. Trans. A*, vol. 22A, no. 3, pp. 685–695, March 1991.

11. Shang, S. S., K. Hokamoto, and M. A. Meyers. "Hot Dynamic Consolidation of Hard Ceramics." *J. Mater. Sci.*, vol. 27, no. 20, pp. 5470–5476, May 1992.

12. Rhinehart, J. S., and J. Pearson. *Explosive Working of Metals*. New York: Macmillan, Inc., pp. 256–257, 1963.

13. Batsanov, S. S. *Effects of Explosions on Materials*. New York: Springer-Verlag, p. 49, 1994.

14. Gabriel, K. A., S. G. Wax, and J. W. McCauley, eds. *Materials Processing by Self-Propagating High-Temperature Synthesis (SHS)*, DARPA/ARMY SHS Symposium Proceedings, MTL-SP-87-3, Daytona Beach, FL, October 1985, United States Printing Office, Washington, DC, 1987.

15. Munir, Z. A. "Synthesis of High-Temperature Materials by Self-Propagating Combustion Methods." *Cer. Bull.*, vol. 67, no. 2, pp. 342–349, February 1988.

16. Munir, Z. A., and J. B. Holt, eds. *Combustion and Plasma Synthesis of High-Temperature Materials*. New York: VCH Publishers, Inc., 1990.

17. Cullity, B. D. *Elements of X-Ray Diffraction*. Reading, MA: Addison-Wesley Publishing Company, Inc., pp. 359–360, 1978.

18. Touloukian, Y. S., ed. *Thermophysical Properties of Matter; Vol. 10. Thermal Diffusivity*. New York: IFI/Plenum, pp. 113 and 198, 1970.

19. Askeland, D. R. *The Science and Engineering of Materials*. Boston, MA: PWS-Kent Publishing Company, 1989.

20. Askill, J. *Tracer Diffusion Data for Metals, Alloys, and Simple Oxides*. New York: Plenum Data Corporation, pp. 52–53, 1970.

21. Weast, R. C., ed. *Handbook of Chemistry and Physics*. 54th Edition, Cleveland, OH: Chemical Rubber Company Press, 1973.

22. Schick, H. L., ed. *Thermodynamics of Certain Refractory Compounds, Vol. I–II*. New York: Academic Press, Inc., 1966.

Appendix A:

Mo-Ti Alloy Molecular Weights and Densities

INTENTIONALLY LEFT BLANK.

Table A-1. Mo-Ti Alloy Molecular Weights and Densities

Molybdenum		Titanium		Mo-Ti	
wt.	at.	wt.	at.	M.W.	Density (g/cm³)
0.000	0.000	1.000	1.000	47.88	4.50
0.100	0.053	0.900	0.947	50.40	4.77
0.200	0.111	0.800	0.889	53.21	5.07
0.300	0.176	0.700	0.824	56.34	5.41
0.400	0.250	0.600	0.750	59.87	5.80
0.500	0.333	0.500	0.667	63.87	6.25
0.550	0.379	0.450	0.621	66.08	6.50
0.600	0.428	0.400	0.572	68.45	6.78
0.650	0.481	0.350	0.519	70.99	7.07
0.700	0.538	0.300	0.462	73.73	7.40
0.710	0.550	0.290	0.450	74.30	7.47
0.720	0.562	0.280	0.438	74.89	7.54
0.730	0.574	0.270	0.426	75.48	7.61
0.740	0.587	0.260	0.413	76.08	7.68
0.750	0.600	0.250	0.400	76.69	7.76
0.760	0.612	0.240	0.388	77.31	7.83
0.770	0.626	0.230	0.374	77.94	7.91
0.780	0.639	0.220	0.361	78.58	7.99
0.790	0.652	0.210	0.348	79.23	8.07
0.800	0.666	0.200	0.334	79.89	8.15
0.810	0.680	0.190	0.320	80.57	8.23
0.820	0.695	0.180	0.305	81.25	8.32
0.830	0.709	0.170	0.291	81.95	8.40
0.840	0.724	0.160	0.276	82.66	8.49
0.850	0.739	0.150	0.261	83.38	8.58
0.860	0.754	0.140	0.246	84.11	8.67
0.870	0.770	0.130	0.230	84.86	8.77
0.880	0.785	0.120	0.215	85.62	8.87
0.890	0.802	0.110	0.198	86.40	8.96
0.900	0.818	0.100	0.182	87.18	9.07
0.910	0.835	0.090	0.165	87.99	9.17
0.920	0.852	0.080	0.148	88.80	9.27
0.930	0.869	0.070	0.131	89.64	9.38
0.940	0.887	0.060	0.113	90.49	9.49
0.950	0.905	0.050	0.095	91.35	9.61
0.960	0.923	0.040	0.077	92.23	9.72
0.970	0.942	0.030	0.058	93.13	9.84
0.980	0.961	0.020	0.039	94.05	9.96
0.990	0.980	0.010	0.020	94.98	10.09
1.000	1.000	0.000	0.000	95.94	10.22

INTENTIONALLY LEFT BLANK.

Appendix B:

W-Ti Alloy Molecular Weights and Densities

INTENTIONALLY LEFT BLANK.

Table B-1. W-Ti Alloy Molecular Weights and Densities

Tungsten		Titanium		W-Ti	
wt.	at.	wt.	at.	M.W.	Density (g/cm³)
0.000	0.000	1.000	1.000	47.88	4.50
0.100	0.028	0.900	0.972	51.70	4.88
0.200	0.061	0.800	0.939	56.19	5.32
0.300	0.100	0.700	0.900	61.53	5.85
0.400	0.148	0.600	0.852	67.99	6.49
0.500	0.207	0.500	0.793	75.97	7.30
0.550	0.241	0.450	0.759	80.70	7.78
0.600	0.281	0.400	0.719	86.07	8.33
0.650	0.326	0.350	0.674	92.20	8.97
0.700	0.378	0.300	0.622	99.27	9.71
0.710	0.389	0.290	0.611	100.82	9.87
0.720	0.401	0.280	0.599	102.41	10.04
0.730	0.413	0.270	0.587	104.06	10.22
0.740	0.426	0.260	0.574	105.76	10.40
0.750	0.439	0.250	0.561	107.51	10.59
0.760	0.452	0.240	0.548	109.33	10.78
0.770	0.466	0.230	0.534	111.21	10.98
0.780	0.480	0.220	0.520	113.15	11.19
0.790	0.495	0.210	0.505	115.16	11.41
0.800	0.510	0.200	0.490	117.25	11.63
0.810	0.526	0.190	0.474	119.41	11.87
0.820	0.543	0.180	0.457	121.66	12.11
0.830	0.560	0.170	0.440	123.99	12.37
0.840	0.578	0.160	0.422	126.41	12.63
0.850	0.596	0.150	0.404	128.92	12.91
0.860	0.615	0.140	0.385	131.54	13.20
0.870	0.635	0.130	0.365	134.27	13.50
0.880	0.656	0.120	0.344	137.12	13.82
0.890	0.678	0.110	0.322	140.08	14.15
0.900	0.701	0.100	0.299	143.18	14.50
0.910	0.725	0.090	0.275	146.42	14.87
0.920	0.750	0.080	0.250	149.81	15.25
0.930	0.776	0.070	0.224	153.36	15.66
0.940	0.803	0.060	0.197	157.08	16.09
0.950	0.832	0.050	0.168	160.99	16.54
0.960	0.862	0.040	0.138	165.09	17.02
0.970	0.894	0.030	0.106	169.41	17.53
0.980	0.927	0.020	0.073	173.96	18.07
0.990	0.963	0.010	0.037	178.77	18.64
1.000	1.000	0.000	0.000	183.85	19.25

INTENTIONALLY LEFT BLANK.

Appendix C:

Calculation of Component Heat Capacities and Enthalpies

INTENTIONALLY LEFT BLANK.

The heat capacity as a function of temperature of each component is obtained from an empirical relation given by Equation C-1. In turn, using the thermodynamic data in Table C-1 with the coefficients listed in Table C-2, the component enthalpies can then be determined in a straightforward manner.

$$C_p = a + (b \times 10^{-3})\, T + C \times 10^{-6})\, T^2 + (d \times 10^5)\, T^{-2}. \qquad (C-1)$$

Table C-1. Thermodynamic Constants for the Components

Component	Phase Transition	Temperature (°C)	Latent Heat (kcal/g)
Ti	α (HCP) $\rightarrow$ β (BCC)	882.	0.95
Ti	β (BCC) $\rightarrow$ liq.	1670.	4.6
Ti	liq. $\rightarrow$ vap.	3550.	101.
Mo	α (BCC) $\rightarrow$ liq.	2620.	6.65
W	α (BCC) $\rightarrow$ liq.	3380.	8.42
TiC[a]	α (FCC) $\rightarrow$ liq.	2940.	20.

Notes: HCP - hexagonal close packed
BCC - body-centered cubic
FCC - face-centered cubic
liq. - liquid
vap. - vapor
[a]All of the listed data are from Weast[1] with the exception of TiC, which is from Schick.[2]

[1] Weast, R. C., ed. *Handbook of Chemistry and Physics.* 54th Edition, Cleveland, OH: Chemical Rubber Company Press, 1973.

[2] Schick, H. L., ed. *Thermodynamics of Certain Refractory Compounds, Vol. I–II.* New York: Academic Press Inc., 1966.

Table C-2. Heat Capacity Coefficients of the Components

Component	Phase	Heat Capacity Coefficients (cal/gmole)			
		a	b	c	d
C	sol.	4.1	1.02	—	−2.1
Ti	α	5.25	2.52	—	—
Ti	β	7.5	—	—	—
Ti	liq.	7.8	—	—	—
TiC[a]	sol.	11.83	0.8	—	−3.58
Mo	sol.	5.48	1.3	—	—
W	sol.	5.74	0.76	—	—

Notes: sol. - solid
       liq. - liquid
[a]All of the listed data are from Weast[1] with the exception of TiC, which is from Schick.[2]

[1] Weast, R. C., ed. *Handbook of Chemistry and Physics.* 54th Edition, Cleveland, OH: Chemical Rubber Company Press, 1973.

[2] Schick, H. L., ed. *Thermodynamics of Certain Refractory Compounds, Vol. I–II.* New York: Academic Press Inc., 1966.

Appendix D:

Thermal Diffusivity of Mo and W

INTENTIONALLY LEFT BLANK.

Table D-1. Thermal Diffusivity of Mo and W

Temperature		Thermal Diffusivity (cm²/s)		a_{Mo}/a_W
(K)	(C)	a_{Mo}	a_W	
100	−173	1.250	1.210	1.033
150	−123	0.746	0.873	0.855
200	−73	0.630	0.764	0.825
250	−23	0.573	0.703	0.815
300	27	0.543	0.662	0.820
350	77	0.521	0.626	0.032
400	127	0.503	0.595	0.845
500	227	0.475	0.542	0.876
600	327	0.451	0.508	0.888
700	427	0.432	0.479	0.902
800	527	0.415	0.454	0.914
900	627	0.396	0.434	0.912
1,000	727	0.376	0.416	0.904
1,100	827	0.357	0.401	0.890
1,200	927	0.339	0.388	0.874
1,300	1,027	0.322	0.375	0.859
1,400	1,127	0.306	0.364	0.841
1,500	1,227	0.293	0.354	0.828
1,600	1,327	0.282	0.345	0.817
1,700	1,427	0.271	0.336	0.807
1,800	1,527	0.262	0.328	0.799
1,900	1,627	0.253	0.320	0.791
2,000	1,727	0.246	0.313	0.786
2,200	1,927	0.232	0.300	0.773
2,400	2,127	0.220	0.289	0.761
2,600	2,327	0.210	0.279	0.753
2,800	2,527	0.202	0.270	0.748
2,900	2,627	0.199	—	—
3,000	2,727	—	0.263	—
3,500	3,227	—	0.249	—

INTENTIONALLY LEFT BLANK.

NO. OF COPIES	ORGANIZATION	NO. OF COPIES	ORGANIZATION

4   CDR
US ARMY RSRCH OFC
DR I AHMAD
DR E CHEN
DR A CROWSON
DR R REEBER
PO BOX 12211
RESEARCH TRIANGLE PARK NC
27709-2211

2   CDR US ARMY ARDEC
AMSTA AR TDC
DR S CYTRON
MR D KAPOOR
PICATINNY ARSENAL NJ
07806-5000

1   CDR
US ARMY NGIC
J CRIDER
W MARLEY
220 SEVENTH ST NE
CHARLOTTESVILLE VA 22901

1   NAT BUREAU OF STANDARDS
DR S J SCHNEIDER
RM A257 BLDG 223
WASHINGTON DC 20234

2   DIR
LAWRENCE LIVERMORE NAT LAB
DR J HOLT L 369
DR D MAIDEN MS L71
PO BOX 808
LIVERMORE CA 94550

3   IDAHO NAT ENG LAB
DR B RABIN
DR G KORTH
DR R WRIGHT
PO BOX 1625
IDAHO FALLS ID 83415

1   BATTELLE
V LINSE
505 KING AVE
COLUMBUS OH 43201

1   BATTELLE PNL
W GURWELL
PO BOX 999
RICHLAND WA 99352

1   CA INST OF TECH
DR T VREELAND
KECK LABS MS 138 78
PASADENA CA 91125

2   CERACON INC
DR R RAMAN
1101 N MARKET BLVD STE 9
SACRAMENTO CA 95834

1   CDR
DARPA
DR P PARRISH
3701 N FAIRFAX DR
ARLINGTON VA 22203-1714

2   GEORGIA INST OF TECHNOLOGY
DR K LOGAN
DR N THADHANI
ATLANTA GA 30332

3   NM INST OF MINING & TECH
CTR FOR EXPLOSIVE TECH
& RSRCH
DR A MILLER
DR P PERSSON
SOCORRO NM 87801

1   NM INST OF MINING & TECH
DEPT OF METALLURGICAL &
MATERIALS ENGRNG
DR O INAL
SOCORRO NM 87801

1   OSRAM SYLVANIA INC
CHEM & METALLURGICAL DIV
DR J MULLENDORE
HAWES ST
TOWANDA PA 18848

1   TELEDYNE FIRTH STERLING
DR S CALDWELL
1 TELEDYNE PL
LAVERGNE TN 37086

NO. OF
COPIES ORGANIZATION

1   GOVT INDUSTRIAL RSRCH INST
     DR N SATA
     4 5 1 NIGATAKE
     MIYAGINO KU
     SENDAI MIYAGI 983 JAPAN

1   NAT RSRCH INST FOR METALS
     DR Y KAIEDA
     2 3 12 NAKAMEGURO
     MEGURO KU
     TOKYO 153 JAPAN

1   OSAKA UNIV
     DR Y MIYAMOTO
     IBARAKI
     OSAKA 567 JAPAN

1   RYUKOKU UNIV
     DR M KOIZUMI
     1 5 YOKOYA
     OE CHO
     OTSU SHIGA 520 21 JAPAN

2   TOKYO INST OF TECH
     DR A SAWAOKA
     DR O ODAWARA
     4259 NAGATSUATA
     MIDORI KU
     YOKOHAMA 227 JAPAN

REPORT DOCUMENTATION PAGE

Public reporting burden for this collection of information is estimated to average 1 hour per response, including the time for reviewing instructions, searching existing data sources, gathering and maintaining the data needed, and completing and reviewing the collection of information. Send comments regarding this burden estimate or any other aspect of this collection of information, including suggestions for reducing this burden, to Washington Headquarters Services, Directorate for Information Operations and Reports, 1215 Jefferson Davis Highway, Suite 1204, Arlington, VA 22202-4302, and to the Office of Management and Budget, Paperwork Reduction Project(0704-0188), Washington, DC 20503.

1. AGENCY USE ONLY *(Leave blank)*	2. REPORT DATE October 1998	3. REPORT TYPE AND DATES COVERED Final, January 1993 - December 1995

4. TITLE AND SUBTITLE
Hot Explosive Consolidation of Molybdenum-Titanium and
Tungsten-Titanium Alloys

5. FUNDING NUMBERS

1L161102AH43
61102A

6. AUTHOR(S)

Laszlo J. Kecskes

7. PERFORMING ORGANIZATION NAME(S) AND ADDRESS(ES)

U.S. Army Research Laboratory
ATTN: AMSRL-WM-TE
Aberdeen Proving Ground, MD 21005-5066

8. PERFORMING ORGANIZATION REPORT NUMBER

ARL-TR-1827

9. SPONSORING/MONITORING AGENCY NAMES(S) AND ADDRESS(ES)

10. SPONSORING/MONITORING AGENCY REPORT NUMBER

11. SUPPLEMENTARY NOTES

12a. DISTRIBUTION/AVAILABILITY STATEMENT

Approved for public release; distribution is unlimited.

12b. DISTRIBUTION CODE

13. ABSTRACT *(Maximum 200 words)*

A novel hot explosive compaction (HEC) technique has been applied to molybdenum (Mo)- and tungsten (W)-based titanium (Ti) alloys. The constituent precursor powders of the alloy billet were surrounded by an exothermic mixture, which, when ignited, released a large amount of heat via a self-propagating high-temperature synthesis (SHS) reaction. Heat from the SHS reaction diffused into the precursor powder bed, causing the interior temperature to rise above 1,500° C. When the powder bed became isothermal, it was consolidated to high density by pressure waves generated by the detonation of an explosive. The amount of explosive charge and the molar ratio of exothermic mixture to sample were adjusted to produce full-density molybdenum-titanium (Mo-Ti) and tungsten-titanium (W-Ti) alloys. The billets were sectioned and examined with scanning electron microscopy (SEM), energy dispersive x-ray spectroscopy (EDS), x-ray diffraction analysis (XRD), and microhardness measurements. In context of the fabrication process, the similarities and differences of the resultant product microstructures are discussed.

14. SUBJECT TERMS
molybdenum, tungsten, titanium, refractory, alloy, microstructure, SHS, combustion synthesis, explosive consolidation, substructural evolution

15. NUMBER OF PAGES
61

16. PRICE CODE

17. SECURITY CLASSIFICATION OF REPORT UNCLASSIFIED	18. SECURITY CLASSIFICATION OF THIS PAGE UNCLASSIFIED	19. SECURITY CLASSIFICATION OF ABSTRACT UNCLASSIFIED	20. LIMITATION OF ABSTRACT UL

INTENTIONALLY LEFT BLANK.

USER EVALUATION SHEET/CHANGE OF ADDRESS

This Laboratory undertakes a continuing effort to improve the quality of the reports it publishes. Your comments/answers to the items/questions below will aid us in our efforts.

1. ARL Report Number/Author___ARL-TR-1827 (Kecskes)___ Date of Report ___October 1998___

2. Date Report Received _____

3. Does this report satisfy a need? (Comment on purpose, related project, or other area of interest for which the report will be used.) _____

_____

_____

4. Specifically, how is the report being used? (Information source, design data, procedure, source of ideas, etc.) _____

_____

_____

5. Has the information in this report led to any quantitative savings as far as man-hours or dollars saved, operating costs avoided, or efficiencies achieved, etc? If so, please elaborate. _____

_____

_____

6. General Comments. What do you think should be changed to improve future reports? (Indicate changes to organization, technical content, format, etc.) _____

_____

_____

_____

CURRENT
ADDRESS

_____
Organization

_____
Name   E-mail Name

_____
Street or P.O. Box No.

_____
City, State, Zip Code

7. If indicating a Change of Address or Address Correction, please provide the Current or Correct address above and the Old or Incorrect address below.

OLD
ADDRESS

_____
Organization

_____
Name

_____
Street or P.O. Box No.

_____
City, State, Zip Code

(Remove this sheet, fold as indicated, tape closed, and mail.)
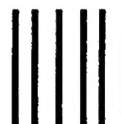**(DO NOT STAPLE)**

DEPARTMENT OF THE ARMY

OFFICIAL BUSINESS

BUSINESS REPLY MAIL
FIRST CLASS PERMIT NO 0001,APG,MD

POSTAGE WILL BE PAID BY ADDRESSEE

DIRECTOR
US ARMY RESEARCH LABORATORY
ATTN AMSRL WM TE
ABERDEEN PROVING GROUND MD 21005-5066